Geochemistry, Geophysics, Geosystems
April 2008 ; Volume 9 (4) : Pages 1-25
http://dx.doi.org/10.1029/2007GC001822

An edited version of this paper was published by AGU.

A geomechanical approach for the genesis of sediment undulations on the Adriatic shelf

Nabil SULTAN[1, *], Antonio CATTANEO[1], Roger URGELES[2], Homa LEE[3], Jacques LOCAT[4], Fabio TRINCARDI[5], Serge BERNE[1], Miquel CANALS[2], and Sara LAFUERZA[2].

[1] Ifremer, Département Géosciences Marines, BP 70, Plouzané F-29280, France
[2] GRC Geociències Marines, Dept. d'Estratigrafia Paleontologia i Geociències Marines, University of Barcelona, Barcelona, Catalonia, Spain
[3] United States Geological Survey, Menlo Park, CA, USA
[4] Department of Geology and Geological Engineering, Laval University, Sainte-Foy, QC, Canada G1K 7P4
[5] ISMAR (CNR), v. Gobetti 101, 40129 Bologna, Italy

*: Corresponding author : Sultan N., email address : nabil.sultan@ifremer.fr, fax +33 (0)298 224570

Abstract:

This study is among the first to examine the genesis of the seafloor and subsurface undulations on the Adriatic continental shelf by integrating stratigraphic information and in situ and laboratory geotechnical measurements. Interpretation of sediment behavior is based on a 32-m-long borehole crossing (1) a possible shear plane and (2) a silty clay layer at about 20 m below seafloor (mbsf) on which sediment undulations are rooted and could be interpreted as a potential weak layer succession. Our main results in terms of triggering mechanism for the observed undulations show that under an earthquake, liquefaction and/or failure of the silty-clay sediments (weak layer) leading to deformation of the upper more cohesive sediments is possible only when such a layer is buried by less than 5 m. For greater burial thicknesses, this silty clay becomes stable under the confining lithostatic pressure exerted by the overlying sediment. This work shows that the seafloor and subsurface undulations observed in the study area are most probably the result of an early deformation process of the seafloor followed by a depositional process.

Keywords: Adriatic shelf; earthquake; shear strength; sediment deformation.

1 INTRODUCTION

Undulated sediment features are commonly observed on the seafloor deep below the wave base in muddy prodeltas [Correggiari et al., 2001; Lee et al., 2002; Mosher and Thomson, 2002; Cattaneo et al., 2004; Urgeles et al., 2007]. Some authors argue that those features are sediment waves induced by bottom currents and/or hyperpycnal flows [e.g., Trincardi and Normark, 1988; Bornhold and Prior, 1990; Lee et al., 2002; Berndt et al., 2006; Urgeles et al., 2007], others identify those areas as sediment deformation structures, creep and/or early signs of slope instability [e.g., Lee et al., 1981; Field and Barber., 1993; Baraza and Ercilla, 1996; Chiocci et al., 1996; Gardner et al., 1999; Correggiari et al., 2001], or as a result of a combination of deformation and depositional processes [Faugères et al., 2002; Gonthier et al., 2002; Cattaneo et al., 2004]. This debate has been especially intense in areas such as the

"Humboldt Slide" offshore California [*Lee et al.*, 2002] illustrating how little is known about the origin and evolution of these undulated sediment features since none of the proposed theories can be easily confirmed or refuted.

Sediment undulations on continental shelves are interesting because they are characterized by relatively recent sedimentation and high human impacts. A correct interpretation and understanding of such features is necessary for a proper risk evaluation (in case of sediment instability) and safe offshore development. Noteworthy is that in continental shelf settings these features occur in areas off river outlets, such as prodeltas, characterized by high sedimentation rates and gas-charged sediments as, for example, the Tiber River prodelta off Rome [*Trincardi and Normark,* 1988; *Chiocci et al.,* 1996], the Noeick River prodelta [*Bornhold and Prior,* 1990], the Gulf of Cadiz [*Baraza and Ercilla,* 1996; *Lee and Baraza,* 1999], and the Llobregat River prodelta off Barcelona [*Urgeles et al.*, 2007]. In the Adriatic, offshore Ortona, the sediment undulations are not only accompanied by free gas in the sediment and relatively high-sedimentation rates, but are also located in an area of frequent earthquake activity that might have acted as a triggering mechanism for deformation [*Correggiari et al.*, 2001].

In many areas of the Western Mediterranean Sea, sediment undulations have been described as being rooted at the last Maximum Flooding Surface (mfs) [*Díaz and Ercilla,* 1993; *Ercilla et al.*, 1995; *Chiocci et al.*, 1996; *Correggiari et al.*, 2001; *Cattaneo et al.*, 2004; *Urgeles et al.*, 2007], and this remarkable sedimentary surface, marking the onset of the present sea level highstand at the base of modern prodeltas, could represent a change in the physical properties of the sediment and a possible explanation for the origin of the undulations. The maximum flooding surface at the Adriatic site is particularly well imaged on seismic reflection profiles, has been correlated regionally and was sampled at several distal locations where prodelta deposits thin out. Here we show, for the first time and thanks to a drilling operation

(PROMESS 1 - June-July 2004), a continuous sedimentary record through this surface at exactly the site where sediment undulations have their maximum expression.

We used undisturbed samples from the PROMESS1 borehole and cone penetration tests to evaluate the mechanical properties of the sediment within the undulated sediment section and at its base. We then modeled the effect of an earthquake of plausible magnitude for this site to reconstruct the mechanical behavior of the sedimentary units within and below the undulations.

The drilling site PRAD2 was selected in the central segment of western Adriatic margin, immediately off Ortona (Figure 1), in an area characterized by seafloor and subsurface undulations. At this site, sediment deformation and/or submarine currents are likely to have a major impact on the observed sedimentary features. *In situ* geotechnical measurements and sediment samples were recovered from this site in order to characterize 1) possible shear planes affecting the Adriatic prodelta mud wedge; and 2) the base of the mud wedge, the maximum flooding surface interpreted as a potential weak layer along which deformation of the above sedimentary units might occur [*Trincardi et al.*, 2004].

2 GEOLOGICAL CONTEXT AND SEAFLOOR FEATURES

The Adriatic region represents a foreland basin formed during the Cenozoic, as a consequence of the convergence between the African and European plates [*Channel et al.*, 1979]. The Apennine chain was built in this geodynamic context and consists of an arcuate thrust belt with convexity toward the Adria-Africa foreland, where the thrusts show different size and curvature that progressively change their orientation [*Cinti et al.*, 2004]. Seismicity is concentrated in the central and southern Apennines. At about 200 km west of the study area, a highly seismically-active central Apennine zone (Umbria) is characterized by moderate magnitude (M < 6) and rare large magnitude (M > 6) earthquakes [*CPTI Working Group*, 1999, 2004]. At about the same distance towards the SE (Figure 1), historical and recent seismicity is documented north of the Gargano promontory with low magnitude (M < 4) earthquakes [*Console et al.,* 1993]. An evaluation of the tectonic activity recorded offshore in the central Adriatic is in *Ridente and Trincardi* [2006].

Late Quaternary deposits on the Adriatic shelf record glacio- eustatic cycles; the most recent of these sequences formed during the last ca. 20 kyr, when a rapid sea-level rise shifted the shoreline from the lowstand position of the Last Glacial Maximum to the modern highstand location. In the central Adriatic, several transgressive and highstand deposits have elongated depocenters along the coast as a consequence of the location of the main sediment entry points (the Po river and several smaller Apennine rivers) and a counter-clockwise circulation [*Cattaneo and Trincardi,* 1999].

During the late Holocene, a progradational mud wedge up to 35 m in thickness deposited along the western side of the Adriatic basin. This mud wedge has an overall clinoform geometry with a submerged offlap break in ca. 25 m water depth and deposited on a flat surface, whereas the average slope angle of the foresets is 0.5 degree. The mud wedge is composed of a basal unit (ca. 1 m thick) overlain by three sigmoidal prograding units; the base of the mud wedge is a regional downlap surface that represents the time of maximum sea level highstand dated ca. 5.5 ka BP [*Correggiari et al.,* 2001]. Shallow gas of biogenic provenance was sampled at several locations along the mud wedge, in association with acoustic masking of seismic-reflection profiles [*García- García et al.,* 2007].

Over large areas (more than 250 km parallel to the coast, between ca 30 and 110 m water depth), the basal unit is acoustically transparent and topped by a discontinuous reflector showing lateral variations in seismic amplitude, likely because of the presence of shallow gas and fluid escape [*Trincardi et al.,* 2004]. In these areas, seafloor and subsurface undulations affect the whole stratigraphic section of the mud wedge or selective sub-units [*Correggiari et al.,* 2001]. Seafloor and subsurface undulations occur in water depths of ca 30 to 70 m with strikes that are sub-parallel to the regional bathymetric contours [*Correggiari et al.*, 2001; *Cattaneo et al.*, 2004]. These undulations are associated with small-scale mud reliefs in water depths of 70 to 110 m, with preferred crest orientations that are perpendicular to regional contours [*Marsset et al.*, 2003].

3 GEOTECHNICAL MEASUREMENTS AND METHODS

3.1 *In situ* testing: CPTU

In the Cone Penetration Test (CPTU) a cone, with an instrumented sleeve above it, is pushed through a series of rods into the sediment layers at a constant rate. A continuous measurement is made of the cone resistance *qc*, the sleeve friction *fs*, and the pore pressure u_2 measured by means of a porous filter located immediately behind the cone (called U2 type cone). The electric cones used by Fugro on board the R/V Bavenit during the PROMESS cruise gave a continuous measurement over successive lengths of 3 meters. The geometry of the used cone penetrometer with tip, sleeve and pore pressure filters follows the International Reference Test Procedure for Cone Penetration Testing [*ISSMGE*, 1999].

The primary objective of hole PRAD2-3 was to mechanically characterize one probable shear plane (from a series of possible shear planes) that were identified from seismic reflection data (Figure 1). For this, the soil hydro-mechanical parameters of the first 32 meters of the sediment column were determined using *in situ* CPTU measurements (for location see Table 1). Eleven CPTU sequences around 3 meters each were carried out (Figure 2 and Figure 3). Unfortunately, instrument failure resulted in invalid data for the upper 15 m and a new, deep CPTU hole (PRAD2-6) was drilled at the same site. To guarantee continuous recovery between holes PRAD2-3 and PRAD2-6, the latter was drilled to 18 mbsf. Thus, six CPTU sequences were obtained at this hole.

3.2 Laboratory testing

An experimental program on undisturbed marine sediments from holes PRAD2-5 and PRAD2-6 (for location see Table 1 and Table 2) was also carried out. Its specific aim was to identify the key mechanical and physical parameters of the sediments that form the undulations in the study area so as to determine whether a genesis by deformation of the sediment column is possible or not. The detailed laboratory geotechnical investigations included:

1- Classification tests;
2- Strength tests under static and dynamic loading;
3- Consolidation/permeability tests

3.2.1 Index properties

Classification tests included unit weight and moisture content determinations, grain size analysis and Atterberg limit tests. The results of the classification tests are presented in Figure 4. The unit weight profile presented in Figure 4-a is obtained from the GEOTEK core logging device [MSCL, *www.geotek.co.uk*] based on a gamma ray source and detector for measuring the attenuation of gamma rays through the core. The P-wave velocity profile of Figure 4-c was obtained from a *celerimeter* device allowing direct measurement of the P wave velocity by insertion of two transducers spaced by a known distance into the sediment. The Atterberg limits and plasticity index were determined using a fall cone according to the method of *Feng* [2001].

3.2.2 Strength tests

Shear strengths determined from laboratory tests were regularly performed using the torvane, the fall cone and, the shear vane devices (UU: Unconsolidated Undrained tests). In addition to these tests, static and cyclic triaxial tests (CU: Consolidated Undrained) were carried out on undisturbed samples from holes PRAD2-5 and PRAD2-6 (appendix A1&A2).

3.2.2.1 Static triaxial tests

Shear-strength parameters were measured to assess whether drained or undrained instability could be at the origin of the observed sediment undulations. Intact values of c' (effective cohesion) and φ (internal friction angle) were determined from consolidated undrained (CU) triaxial shearing tests [e.g., *Germaine and Ladd,* 1990] made at various confining pressures (20–100 kPa) on samples from holes PRAD2-5 and PRAD2-6 (appendix A1).

3.2.2.2 Cyclic triaxial tests

Assessing the potential for triggering or initiation of sediment liquefaction and degradation of soft clays under cyclic loading has been a problem of major concern since the early 1960s. Under the effect of an earthquake, the sediment dynamic behavior is influenced by the intensity and duration of the cyclic loading and the state of the sediment (the grain size distribution, the presence or absence of a clay fraction, the consolidation state, and the degree of saturation). Cyclic loading may lead to degradation or cyclic softening failure of soft clays [e.g. *Pestana et al.,* 2000] and the liquefaction of sandy silty sediments [*Ishihara,* 1985]. Liquefaction failure over gentle slope enhances lateral spreading, ground settlement and sometimes generates sand boils [*Varnes,* 1978].

Boulanger and Idriss [2006] have recently defined a new criteria based on the stress-strain behavior for distinguishing between silts and clays that are susceptible to liquefaction versus cyclic softening failure. *Boulanger and Idriss* [2006] show that the transition between liquefaction (sediments that behave more like sands) and cyclic softening failure (sediments that behave more like clays) depends strongly on the plasticity indices (PI) of the sediment. *Boulanger and Idriss* [2006] found that clay-like behaviour (cyclic softening failure) occurs for fine-grained soils that have PI greater or equal to 7. Sediments from PRAD2 borehole (Figure 4) indicate that both liquefaction and cyclic softening failure may occur within the studied sedimentary column.

In order to evaluate the liquefaction/failure potential, two primary seismic variables are required. These variables are the level of cyclic stress induced by the earthquake on a sediment layer, expressed in terms of cyclic stress ratio (CSR), and the capacity of a sediment layer to resist liquefaction and softening failure, expressed in terms of cyclic resistance ratio (CRR).

Evaluation of the cyclic resistance ratio (CRR) has developed along two specific areas of research: methods based on the results of laboratory tests, and methods based on *in situ* tests and field observations of liquefaction behavior in past earthquakes. In laboratory testing, the number of shear stress cycles is the basis for expressing the resistance of sediment to the initiation of liquefaction and cyclic softening failure.

Using the cyclic triaxial test, the Cyclic Resistance Ratio (CRR) corresponds to the cyclic stress ratio amplitude ($=\sigma_{d,cyc}/2\sigma'_{30}$ where $\sigma_{d,cyc}$ is the cyclic deviator stress and σ'_{30} is the effective minor principal stress at the end of consolidation). The potential for liquefaction can then be evaluated by comparing the earthquake loading (CSR) with the liquefaction resistance (CRR). The ratio between both values is the factor of safety against liquefaction.

Fifteen cyclic triaxial tests were carried out at different Cyclic Stress Ratios (CSR) (Table 3) on samples from cores PRAD2-5 and PRAD2-6. Samples were isotropically consolidated to different effective confining pressures. The cyclic tests, carried out in *Fugro-France's* laboratory, aimed to investigate the potential that liquefaction and pore pressure build-up during cyclic loading might have in generating deformation of the prodeltaic sediments. Tests were performed on undisturbed samples from different sedimentary units: the lower sandy layer (level 3 - Figure 4), the silty clay layer above the maximum flooding surface (level 2 -

Figure 4) and the surrounding matrix clayey sediment in order to understand stratigraphic controls in the genesis of the observed features (for more details see appendix A2). In this work, liquefaction is considered to occur for excess pore pressure equal to 90% of the initial confining stress: according to *Ishihara* [1993], silty sands or sandy silts containing some amount of fines may behave as liquefiable materials with an excess pore pressure values equal to 90 to 95 percent of the initial confining stress.

3.2.3 Consolidation/permeability tests

Nine oedometer-consolidation tests were carried out at Site PRAD2 in order to characterize the consolidation state and pore pressure in the sediment column. Oedometer tests were conducted according to the ASTM D-2435 method [*ASTM*, 1993]. The determination of the hydraulic conductivities and permeability coefficients were also possible using the falling head method.

4 CORRELATION BETWEEN GEOTECHNICAL DATA AND THE SEDIMENTARY LAYERS FROM PRAD2 SITE

4.1 From CPTU

Figure 2-a presents the corrected cone resistance q_t versus depth below seafloor of holes PRAD2-3 (from 0 to 15 mbsf) and PRAD2-6 (from 15 mbsf to around 32 mbsf). The geotechnical dataset obtained from the PRAD2 site appears consistent and of good quality. The q_t profile (Figure 2-a) shows: 1) a linear increase with depth until 20.2 mbsf; 2) relatively high q_t values between 20.2 m and 20.9 mbsf, 3) again a linear increase between 20.9 m and 27.5 mbsf and 4) a sudden increase in q_t values at 27.5 mbsf followed by highly oscillating values to the base of the borehole. Figure 2-b presents the unit sleeve friction resistance, *fs*, versus depth below seafloor of holes PRAD2-3 (from 0 to 15 mbsf) and PRAD2-6 (from 15 mbsf to around 32 mbsf). The *fs* profile in Figure 2-b shows a similar trend to that observed

from the q_t profile. Figure 2-c shows the pore pressure u_2 generated by the rod penetration versus depth below seafloor for holes PRAD2-3 and PRAD2-6. The pore pressure profile shows a generally linear increase with two major reductions in the intervals between 20.2 m and 20.9 m and below 27.5 mbsf. The simultaneous variation of q_t, *fs* and *qc* is a typical indicator of the presence of silty sediment at these intervals. Figure 3 shows an enlargement of the interval between 18 m and 24 m below seafloor of CPTU measurements from hole PRAD2-3. CPTU data show a layer between 20.2 mbsf and 20.9 mbsf characterized by relatively high cone resistance, high friction and low excess pore pressure. According to *Robertson* [1990], these features are characteristic of coarser material (silty sediment). In order to recover additional sediment from this particular layer, 1.6 m of sediment were cored at hole PRAD2-6 between 19.75 mbsf and 21.35 mbsf.

4.2 From index properties

Figure 2-d shows the unit weight profile obtained from the core-logger γ-density compared to the unit weight determined from water content values (assuming 100% saturation, PRAD2-5). There is a maximum shift of 0.7 kN/m^3 between the two profiles from the seafloor to 23 mbsf, followed by a very good agreement between the two profiles. The unit weight profiles (Figure 2-d) show a sudden increase at around 25.9 mbsf, which corresponds to a change in sediment type (from finer to coarser). The boundary between these two sediment types was observed at 27.5 mbsf, based on CPTU data at hole PRAD2-3, which is only 9 m distant from PRAD2-5. The increase in unit weight with depth at around 26 mbsf is supported by the grain size distribution profile presented in Figure 4-b (level 3). At this level (level 3), the clay content decreases to around 16% with a silt content of around 60 % and a sand content of around 24 %. Two other levels can also be identified from the grain size distribution profile. The first level (level 1) at around 6 mbsf is characterized by a silt content of around 62 % and a sand

content of around 13 %. The second level at around 20.5 mbsf contains around 53 % silt and 10 % sand.

The water content profile presented in Figure 4-c shows a linear decrease with depth over the first 26 mbsf followed by an important decrease of the water content in the sandy clay layer reaching 20 % at around 28.5 mbsf. The plasticity index profile (Figure 4-e) shows that the sediment from PRAD2 site is characterized by medium plasticity whereas the sediment from level 1 is just slightly plastic. The plasticity index was not determined for level 2 and level 3. The liquidity index profile showing the plastic behavior of the sediment (liquidity index values between 0 and 1) is presented in Figure 4-f and compared to the analytical expression given by *Lévesque* [2005].

Figure 2-e shows the core-logger compressional wave velocity, V_p, versus depth at hole PRAD2-5. The profile shows a sudden decrease below 21.5 mbsf that is probably related to gas exsolution due to the change in pressure and temperature between *in situ* and laboratory conditions. The signal of the P wave was lost below 22.5 m, also probably due to this process. Above 22.5 m, the P-wave velocity values vary between 1481 m/s and 1532 m/s.

Two main reflectors defined from seismic profiles and identified as the transgressive surface (TS) and the maximum flooding surface (mfs) seem to match a sharp increase in q_t at the PRAD2 site (Figure 5), although these increases are slightly less pronounced for the mfs than for the TS. The increase in q_t at the level of the two main reflectors was accompanied by a decrease of the excess pore pressure (Figure 2 and Figure 3), which indicates coarser sediment.

4.3 From shear strength

The undrained shear strength profile presented in Figure 5-a and appendix A1 (Figure A 1) is clearly disrupted at about 11 mbsf with an increase of about 12 kPa. At this depth, drilling penetrated from one sediment undulation to the one immediately upslope, and from the “lee” side of one undulation to the "stoss" side of the next one. A depth offset of about 1 to 2 meters can be observed between the Su peak and the depth of the interface between undulations as identified from the seismic data in Figure 5. This interface did not have an expression on the CPTU measurements.

Figure 6 shows the variation of CRR as a function of the cycles to liquefaction or cyclic softening failure. Comparison between the three curves in Figure 6 shows clearly three different behaviors as explained in appendix A1. Figure 6 illustrates the example of an earthquake of magnitude 6.8 at 50 km epicentral distance with 16 significant cycles according to the empirical regression equations given by *Liu et al.*, [2001]. Figure 6 shows that failure may occur under CSR of 0.36 for level 3 and CSR of 0.46 for level 2. The surrounding clayey sediment cannot fail under an earthquake equivalent to 16 loading cycles.

5 DISCUSSION

5.1 Sedimentation rate, excess pore pressure and consolidation state

In normally pressured geological formations, the sediment is permeable and the fluid can communicate through the different layers. The pore water is free to escape during consolidation; thus the fluid pressure is hydrostatic. For over-pressurized layers, the permeability of the sediment is low and restricts fluid circulation. In these layers, an increase in sediment loading is transferred in part from the sediment matrix to the pore water. Thus, the pore water partially supports the overburden pressure, which prevents the pores from compressing under the weight of the overburden. The normal consolidation phenomenon is retarded and the sediment is in an under-consolidated state.

Figure 7 shows the Over-Consolidation Ratio (*OCR* is defined as the ratio of the preconsolidation stress to the effective stress calculated from the unit weigh profile) derived from the oedometer tests indicating that the sediment is in an under-consolidated state. Two different under-consolidation states can be clearly identified from Figure 7 where the *OCR* is between 0.9 and 1 for the upper 4 points (between the seafloor and 8 mbsf) and under-consolidated for the lower 3 points (below 14 mbsf). The results are qualitatively supported by consolidation state estimates carried out using Skempton's equation [*Skempton*, 1954], which relates the consolidation state to the undrained shear strength and plasticity indices. Using this *Skempton* [1954] approach, the consolidation profile shows nearly normally consolidated to slightly over-consolidated sediments within the upper part of the sedimentary column, whereas under-consolidated sediments are present in the lower part of the profile. The consolidation state profile derived from Skempton's equation shows overconsolidated sediment (*OCR* about 2,7) at about 11 mbsf, coinciding with the location of the plane that separates one sediment undulation from another (Figure 1).

From the sedimentation rate, the porosity, the permeability and the bulk unit weight of the sediment, it is also possible to estimate theoretically the evolution of excess pore pressure and stress state over the sediment column. In order to evaluate the origin of overpressures in the Adriatic sedimentary column, we used the SeCo software, [*Sultan et al.*, 2004 and *Leynaud et al.*, 2007] which solves consolidation equation using a finite difference model.

The SeCo software uses an upper moving boundary, simulating continuous sedimentation, in combination with the principle of effective stress (σ'_v), which in porous media is the difference between the total stress (σ_v) and the pore fluid pressure (u). The link between the void ratio *e* and the vertical effective stress is considered through the compression index (see Figure 8-b), whereas the permeability coefficient depends on the void ratio through the theoretical permeability curve (see Figure 8-c).

The process of consolidation is directly related to the rate of excess pore pressure dissipation and the rate of sedimentation. The key equation used to evaluate the evolution of the excess pore pressure during the sedimentation process is the consolidation equation [*Terzaghi and*

Peck, 1967]. Figure 8-a shows the excess pore pressure at site PRAD2 versus depth derived from oedometer tests and that calculated using the SeCo software [*Sultan et al.,* 2004] for two different sedimentation rates characterizing the study area (5 m.kyr^{-}1 and 10 m.ky^{-1} – from *Vigliotti et al.,* 2008). The results from this theoretical analysis (Figure 8) show that the sedimentation rate in the study area is too low to generate excess pore pressures as high as those measured in the consolidation tests. The excess pore pressure predicted from the observed sedimentation rate is too low to trigger alone instability and/or deformation that could account for the observed mud reliefs. However, an important mechanism that could contribute significantly to the excess pore pressure is earthquake shaking, which would also promote sediment remolding.

5.2 Earthquakes and liquefaction development as possible source of sediment deformation

5.2.1 Historical seismicity

The seismicity of the area is well known both from reports of strong historical earthquakes and from seismic sequences that have been recorded over the last few decades [*Trincardi et al.,* 2004]. Focal regions on land and offshore cluster along the main tectonic structures described above, reaching magnitudes typically between 5 and 6 on the Richter scale [*Tinti et al.,* 1995; *Tinti and Armigliato,* 2003]. Earthquakes located offshore of the Gargano Promontory display very high energy releases with peaks greater than Richter magnitude 6.6; the largest seismic events have an estimated return interval of 228 years [*Tinti et al.,* 1995]. Major destructive earthquake shocks in historical times occurred in 1223, 1627 and 1731 AD [*Postpischl,* 1985]. According to *Trincardi et al.* [2004] and because much of the seismic activity is located offshore, the central Adriatic has been affected by large historical tsunamis, of which the 1627, 1646, 1731 AD and December 8, 1889 were the most devastating [*Tinti et al.*, 1995].

Figure 9-a summarizes the historical seismicity in the area during the last 400 years. Only significant magnitudes (>5) have been considered and plotted in Figure 9, showing that maximum earthquake magnitude during the last 400 years is around 7. Palaeoseismic studies of faults in the central Apennine region suggest that this value was not exceeded during the Holocene [*Pantosti et al.*, 1996; *Galadani and Galli*, 1999]. From the earthquake magnitudes and their respective distance to the study area, the Peak Ground Acceleration (*PGA*) was evaluated using Idriss' method [*Idriss*, 1993], which proposes relationships for *PGA* for various magnitudes (M) in the range from 4.5 to 8.5. The relationship depends on epicentral distance for M ≥ 6 and hypocentral distance in km otherwise. In Figure 9-b the calculated *PGA* for two different fault mechanisms (reverse and strike slip) is presented. The two maximum *PGA*s that the study area has been subject to during the last 400 years are 0.08g in 1706 and 0.075g in 1881. The calculated *PGA* fit with the range (0.08g – 0.16g) given by the Global Seismic Hazard Assessment Program [*http://www.seismo.ethz.ch/gshap/adria/*] for the Adriatic Sea and for a 475 year return period.

5.2.2 A representative seismic ground motion record

Within the frame of the European project COSTA (2000-2003), an Ocean Floor ObServatory (OFOS) was deployed in order to investigate the effect of earthquakes on pore pressure in the upper soft sediment of the Adriatic continental shelf [*Mienert et al.*, 2002]. With the OFOS two instruments were deployed: a 3-component Ocean Bottom Seismometer (OBS) for recording the seismic events and a PUPPI (Pop-Up Pore Pressure Instrument) to measure the pore pressure transients that might occur in the sediments in relation to a possible earthquake event [*Schultheiss et al.*, 1985].

The OFOS deployment (42°25.1701'N and 14°26.4872'E) took place about 8 km offshore the port of Ortona (Italy) in 31.4 m water depth (Figure 1). The OFOS recorded *in situ* data for about one year (from the 16th of May 2001 to the 15th of April 2002). However, after recovery, it turned out that the PUPPI had been damaged, and only the OBS seismic data were properly recorded. Due to the sensitivity of the OBS, it was only possible to record events within a range of 250 km from deployment location. One of the most important seismic events that occurred within that range was an earthquake on July 2, 2001 (Table 4). The magnitude and *PGA* generated by the earthquake of July 2001 are shown in Figure 9-a and Figure 9-b. The distance from the epicenter to the OFOS instrument was approximately 88 km. In this work, the *PGA* for a return period of 475 years and the seismogram of the event of July 2, 2001 was used to simulate the effect of earthquake shaking on the sedimentary column. It is important to mention that the use of a small earthquake event (M=4.2), even normalized to an accurate *PGA*, represents a source of uncertainty in the calculation results which is mainly related to the frequency and duration of an earthquake. *Biscontin and Pestana* [2006] have shown the importance of "selecting representative ground motions that include realistic combinations of distance, maximum horizontal acceleration and duration".

5.2.3 Effect of earthquake loadings on excess pore pressure and sediment deformation

Simulations of the effect of earthquake shaking on possible deformation from build-up of the pore pressure within the different sedimentary layers were carried out using Cyclic1D software [*http://cyclic.ucsd.edu*]. Cyclic1D is a non-linear finite element program for execution of one-dimensional site amplification and liquefaction simulations (for level as well as mildly inclined sites). Finite Elements are employed within an incremental plasticity coupled solid-fluid formulation. The liquefaction model employed in Cyclic1D is formulated within the framework of multi-yield-surface plasticity [for more details see *Elgamal et al.*, 2002; *Yang et al.*, 2004].

The model parameters needed in Cyclic1D are the shear wave velocities V_s determined from the cyclic triaxial tests [V_s is a function of the shear modulus G and the unit weight, e.g. *Locat and Beauséjour,* 1987], the friction angle, the Poisson's ratio, the permeability coefficient, the unit weight and the excitation signal. The only geometry parameter used in the calculation is the mean slope angle, which was taken equal to 1.5 degree. The seismogram of July 2001 was normalized to a *PGA* of 0.08g and used to simulate the effects of earthquake shaking on the sedimentary column at site PRAD2.

The sedimentary column at the PRAD2 site was divided into 6 layers, according to the hydro-mechanical parameters obtained from the different *in situ* and laboratory geotechnical tests (Table 5). The initial pore pressure was considered equal to the hydrostatic pressure. Figure 10 shows the seismogram recorded by OFOS [*Mienert et al.,* 2002] and used in the calculation (a) and the calculation results in terms of excess pore pressure (b), effective stress (c) and CSR (d) versus depth. CRR values obtained from the cyclic trixial tests carried out on sediments from level 2 and level 3 are added to Figure 10-d. Sediments from level 1 (as defined in Figure 4-b) were not tested under cyclic triaxial tests, however from the plasticity index and the grain size distribution, its behavior was considered similar to that of level 2. Under the earthquake seismogram recorded by OFOS [*Mienert et al.,* 2002] and shown in Figure 10-a, the most sensitive layer seems to be level 1 where the excess pore pressure at the end of the earthquake shaking raised above 90 % of the lithostatic stress. The critical CRR values obtained from the triaxial cyclic tests carried out on samples from level 2 and level 3 are added to Figure 10-d and show that the excess pore pressure generated within levels 2 and 3 remains too low to generate liquefaction and/or the failure of those two levels. The initial excess pore pressure considered equal to the hydrostatic pressure for the 6 sedimentary layers could be a source of uncertainty in the present calculation results. However, in the absence of accurate measurements of the *in situ* excess pore pressure it is not possible to evaluate the uncertainty in the modeling results. The simulation results presented in Figure 10 and the comparison between CRR and CSR values presented in Figure 10-d show that for the present day stratigraphy and for the maximum historical earthquake, only the upper silty layer (level 1) could liquefy. On the other hand, it seems that the sediment undulations are rooted at the mfs (top of level 2; Figure 1–b), not at level 1. This indicates that deposition of level 1 most probably occurred after formation of the undulations took place.

Three additional analyses were carried out using the Cyclic1D software to define the critical depth of level 2 during deposition history at which an earthquake of similar frequency content and duration to that of July 2001 [*Mienert et al.*, 2002], but scaled to the maximum *PGA* observed during the last 400 years, would be able to produce deformation of the sedimentary column above it. Figure 11 shows the simulation results in terms of normalized excess pore pressure with respect to the vertical effective stress for the three investigated depths of level 2 (Figure 11-a: 10.5 mbsf, Figure 11-b: 5.5 mbsf and Figure 11-c: 3 mbsf). For the three calculations the ratio of the excess pore pressure to the vertical effective stress after the earthquake shaking was equal to 0.8, 0.87 and 0.94, respectively. The simulation results presented in Figure 11 show that under an earthquake similar to that presented in Figure 10-a the liquefaction and/or failure of layer 2, inducing deformation of the upper clayey sediments, could only occur for as long as this layer was buried with less than 5 m of sediment. For greater burial thicknesses, this silty clay layer becomes stable because of the confining lithostatic pressure of the overlying sediment. Moreover, a classical deformation process (Mohr-Coulomb failure) related to gravitational loading cannot explain the observed undulations in the area [*Berndt et al.*, 2006]. These observations and calculation results, show that the seafloor and subsurface undulations are most probably the result of an early deformation that has predisposed the seafloor for a subsequent sediment wave style deposition.

The potential liquefaction of sediments from level 2 cannot explain, however, the origin of the excess pore pressure identified from the *in situ* measurements and laboratory testing. An open question remains about the role of free gas identified from seismic data (Figure 1-b) in generating the observed excess pore pressures.

6 CONCLUSION

The integration of stratigraphic information (geometry, sedimentary facies, chronology), *in situ* geotechnical measurements (CPTU), laboratory measurements of physical and mechanical sediment properties (classification tests, oedometer/permeability, static and cyclic triaxial compression tests) allowed a rigorous analysis of the mechanical behavior of the Adriatic prodeltaic sediments and an assessment of its response to seismic ground motions. The main conclusions that can be drawn from this study are:

- The existence of a boundary at 9 mbsf between low and high undrained shear strength (*Su)*. This limit fits well with the interface (at around 8 mbsf) between one package of undulations (belonging to a seismic unit showing high values of reflection amplitude on CHIRP sonar profiles) and an underlying package.The existence at 20.5 mbsf of a silty clay layer, interpreted as the basal unit of the late Holocene mud wedge immediately above the mfs, with coarser grain size than the underlying and overlying units. This layer was identified from *in situ* measurements as well as laboratory testing;
- Oedometer tests have shown that sediment from the PRAD2 site is slightly under-consolidated to normally consolidated in the upper part of the borehole (above 8 m) and highly under-consolidated in the lower part (below 14 m).
- Cyclic triaxial tests show two different dynamic behaviors characterizing the Adriatic prodeltaic sediment: one for granular silty-clay, silty or sandy sediment (liquefaction), another for cohesive clay sediment (cyclic softening failure). From the triaxial cyclic

tests and the *in situ* effective stress measurements it is clear that the silty/sandy sediment is the most sensitive to earthquake loading.

- Modeling results indicate that the origin of the excess pore pressure identified from *in situ* measurements and laboratory testing seems unrelated to the high sedimentation rate and/or to the high seismicity in the area. Therefore, an open question remains about the role of the free gas in generating the observed excess pore pressure.
- Calculation of the potential for liquefaction and degradation of sediments from PRAD2 site, under an earthquake similar in frequency and duration to the that of July 2001 and for a maximum *PGA* of 8% g, shows that sediment liquefaction within level 2 (layer above the mfs at which the undulations are rooted), and deformation of the above sedimentary column, could only be possible up to a maximum level 2 burial of 5 meters. For greater burial thicknesses, level 2 silty clay becomes stable because of the confining lithostatic pressure of the overlying sediment. This work shows that in the study area the seafloor and subsurface undulations are most probably the result of an early deformation of the seafloor that has predisposed the seafloor for a subsequent sediment wave style deposition.

ACKNOWLEDGEMENTS

This study has been possible thanks to EC project PROMESS1 (contract EVR1-CT- 2002-40024) and EURODOM (contract RTN2-2001-00281). OFOS data were acquired within the EC project COSTA (EVK3-CT-1999-00006) and were made available by J. Mienert and C. Berndt. R.U. acknowledges “Ramón y Cajal” contract by the Spanish “Ministerio de Educación y Ciencia”.

REFERENCE

ASTM (1993), Standard Test Method for One-Dimensional Consolidation Properties of Soils, *Annual Book of ASTM Standards*, *D2345-90*, *04-08*, 313-323.

Baraza, J., and G. Ercilla (1996), Gas-charged sediments and large pockmark-like features on the Gulf of Cadiz slope (SW Spain), *Marine and Petroleum Geology*, *13*, 253-261.

Berndt, C., A. Cattaneo, M. Szuman, F. Trincardi, and D.G Masson (2006), Sedimentary structures offshore Ortona, Adriatic Sea - deformation or sediment waves?, *Marine Geology*, *234*, 261-270. (doi:10.1016/j.margeo.2006.09.016).

Biscontin, G., and J.M. Pestana (2006), Factors affecting seismic response of submarine slopes, Natural Hazards and Earth System Sciences, 6, 97-107.

Bornhold, B. D., and D. B. Prior (1990), Morphology and sedimentary processes on the subacqueous Noeick river delta, British Columbia, Canada, in *Coarse-grained Deltas, Spec. Publ. 10*, edited by A. Colella and D. B. Prior, pp. 169– 184, Int. Assoc. of Sedimentol., Oxford, UK.

Boulanger, R.W., and I.M. Idriss (2006), Liquefaction Susceptibility Criteria for Silts and Clays, *J. Geotech. and Geoenvir. Engrg.*, *132*, 1413-1426.

Cattaneo, A., and F. Trincardi (1999), The late- quaternary transgressive record in the Adriatic Epicontinental Sea: basin widening and facies partitioning, in *Isolated Shallow Marine Sand Bodies: Sequence Stratigraphic Analysis and Sedimentologic Interpretation*, edited by K.M. Bergman and J. Snedden, J., *SEPM Special Publication*, *64*, 127-146.

Cattaneo, A., A. Corregiari, T. Marsset, Y. Thomas, B. Marsset, and F. Trincardi (2004), Seafloor undulation pattern on the Adriatic shelf and comparison to deep-water sediment waves, *Marine Geology*, *213*, 121-148.

Channell, J.E.T., B. D'Argenio, and F. Horvath (1979), Adria, the African Promontory, in Mesozoic Mediterranean paleogeography, *Earth Science Reviews*, *15*, 213-292.

Chiocci, F. L., F. Esu, P. Tommasi, and V. Chiappa (1996), Stability of the submarine slope of the Tiber River delta, in *Landslides*, edited by K. Senneset, pp. 521– 526, Balkema, A. A., Brookfield, Vt.

Cinti, F.R., L. Faenza, W. Marzocchi, and P. Montone (2004), Probability map of the next M ≥ 5.5 earthquakes in Italy, *Geochemistry Geophysics Geosystems, 5*, Q11003, doi:10.1029/2004GC000724.

Console, R., R. Di Giovanbattista, and P. Favali (1993), Seismicity of the Adriatic microplate, *Tectonophysics*, *218*, 343-354.

Correggiari, A., F. Trincardi, L. Langone, and M. Roveri (2001), Styles of failure in late Holocene highstand prodelta wedges on the Adriatic shelf, *J. Sediment. Res*, *71*, 218–236.

CPTI Working Group (1999), Catalogo parametrico dei terremoti Italiani, GNDT-ING-SGA-SSN, 88 pp., Ist. Naz. di Geofis. e Vulcanol., Bologna, July. (Available at http:// emidius.mi.ingv.it/CPTI).

CPTI Working Group (2004), Catalogo parametrico dei terremoti Italiani, version 2004 (CPTI04), Ist. Naz. di Geofis. e Vulcanol., Bologna. (Available at http://emidius.mi.ingv.it/ CPTI).

Díaz, J.I., and G. Ercilla (1993), Holocene depositional history of the Fluvià-Muga prodelta, northwestern Mediterranean Sea, *Mar. Geol.*, *111*, 83-92.

Elgamal, A., Z. Yang, E. Parra (2002), Computational Modeling of Cyclic Mobility and Post-Liquefaction Site Response, *Soil Dynamics and Earthquake Engineering*, *22(4)*, 259-271.

Ercilla, G., J.I. Díaz, B. Alonso, and M. Farrán (1995), Late Pleistocene-Holocene sedimentary evolution of the northern Catalonia continental shelf (northwestern Mediterranean Sea), *Continental Shelf Research*, *15*, 1435-1451.

Faugères, J.-C., E. Gonthier, T. Mulder, N. Kenyon, P. Cirac, R. Grimboulard, S. Berné, and R. Lesuavé (2002), Multi-process generated sediment waves on the Landes Plateau (Bay of Biscay, North Atlantic), *Marine Geology*, *182*, 279– 302.

Feng, T. W. (2001), A linear log d ~ log w model for the determination of consistency limits of soils, *Canadian Geotechnical Journal*, *38*, 1335-1342.

Field, M. E., and J. H. Barber Jr. (1993), A submarine landslide associated with shallow sea-floor gas and gas-hydrates off northern California, in *Submarine Landslides: Selected Studies in the U.S. Exclusive Economic Zone, Surv. Bull. 2002*, edited by W.C. Schwabet al., pp. 151–157, U.S. Geol. Soc., Washington DC.

Galadini, F., and P. Galli (1999), The Holocene paleoearthquakes on the 1915 Avezzano earthquake faults (central Italy): Implications for active tectonics in the central Apennines, *Tectonophysics*, *308*, 143-170.

García-García, A., D.L. Orange, S. Miserocchi, A. Correggiari, L. Langone, T.D. Lorenson, F. Trincardi, and C.A. Nittrouer (2007), What controls the distribution of shallow gas in the Western Adriatic Sea?, *Continental Shelf Research*, *27*, 359-374.

Gardner, J.V., D.B. Prior, and M.E. Field (1999), Humboldt slide – a large shear-dominated retrogressive slope failure, *Marine Geology*, *154*, 323-338.

Germaine, J.T., and C.C. Ladd (1990), Triaxial testing of saturated cohesive soils, *ASTM Spec. Tech. Publ.*, *977*, 421-459.

Gonthier, E., J.-C. Faugères, A. Gervais, G. Ercilla, B. Alonso, and J. Baraza (2002), Quaternary sedimentation and origin of the Orinoco sediment-wave field on the Demerara continental rise (NE margin of South America), *Marine Geology*, *192*, 189– 214.

Idriss, I. M. (1993), *Procedures for selecting earthquake ground motions at rock sites*. Tech. rept. NIST GCR 93-625. National Institute of Standards and Technology.

Ishihara, K. (1985), Stability of natural deposits during earthquakes, in 1*1th International Conference on Soil Mechanics and Foundation Engineering*, pp. 321–376, San Francisco,

Ishihara, K. (1993), Liquefaction and flow failure during earthquakes, *Geotechnique*, *43*, 351-415.

ISSMGE International Society of Soil Mechanics and Geotechnical Engineering (1999), International Reference Test Procedure for the Cone Penetration Test (CPT) and the Cone Penetration Test with Pore Pressure (CPTU), Report of the ISSMGE Technical Committee 16 on Ground Property Characterisation from In-Situ Testing, Proceedings of the Twelfth European Conference on Soil Mechanics and Geotechnical Engineering, Edited by Barends et al., pp. 2195-2222, Amsterdam.

Lee, H., and J. Baraza (1999), Geotechnical characteristics and slope stability in the Gulf of Cadiz. *Mar. Geol.*, *155*, 173-190.

Lee, H. J., B. D. Edwards, and M. E. Field (1981), Geotechnical analysis of a submarine slump, Eureka, California, paper presented at Offshore Technology Conference, Am. Assoc. of Petrol. Geol., Houston, Tex.

Lee, H.J., J.P.M. Syvitsky, G. Parker, D. Orange, J. Locat, J.H.W. Hutton, and J. Imran (2002), Distinguishing sediment waves from slope failure deposits: field examples, including the “Humboldt Slide” and modelling results, *Marine Geology*, *192*, 79-104.

Lévesque, M.C. (2005), Évaluation de l'impact de la bioturbation sur les propriétés physiques des sédiments récents du delta du Pô, Italie, M. Sc. Thesis, 49 pp., Department of Geology and Geological Engineering, Laval University, Canada.

Leynaud, D., N. Sultan, and J. Mienert (2007), The role of sedimentation rate and permeability in the slope stability of the formerly glaciated Norwegian continental margin : the Storegga slide model, *Landslides*, doi 10.1007/s10346-007-0086-z.

Liu, A.H., J.P. Stewart, N.A. Abrahamson and Y. Moriwaki (2001), Equivalent number of uniform stress cycles for soil liquefaction analysis, *Journal of Geotechnical and Geoenvironmental Engineering*, *127*, 1017-1026.

Locat, J., and N. Beauséjour (1987), Correlations entre des proprietes mecaniques dynamiques et statiques de sols argileux intacts et traites à la chaux, *Can. Geotech. J.*, *24*, 327-334.

Marsset, T., B. Marsset, Y. Thomas, P. Cochonat, A. Cattaneo, and F. Trincardi (2003), Detailed anatomy of late Holocene deposits on the Adriatic shelf from 3D very high resolution seismic data (TRIAD survey) in *Advances in Natural and Technological Hazards Research*, edited by J. Locat, and J., Mienert, J., pp. 449– 458, Kluwer, Dordrecht, The Netherlands.

Mienert, J., C. Berndt, S. Bünz, and S. Guidard (2002), Presentation of the OFOS seismic data, cruise report, EC project COSTA (EVK3-CT-1999-00006), 22 pp.

Mosher, D.C., and R.E Thomson (2002), The Foreslope Hills: large-scale, fine-grained sediment waves in the Strait of Georgia, British Columbia, *Marine Geology*, *192*, 275-295.

Pantosti, D., G. D'Addezio, and F.R Cinti (1996), Paleoseismicity of the Ovindoli-Pezza fault, central Apennines, Italy: A history including a large, previously unrecorded earthquake in the Middle Ages (860-1300 A.D.), *Journal of Geophysical Research*, *101*, 5937-5959.

Pestana, J.M., G. Biscontin, F. Nadim, and K. Andersen (2000), Modeling cyclic behavior of lightly overconsolidated clays in simple shear, *Soil Dynam. Earthquake Eng.*, *19*, 501– 519.

Postpischl, D. (1985), Catalog of the Italian earthquakes from 1000 to 1980, *Quaderni de La Ricerca Scientifica, 114-2B.*

Ridente, D., and F. Trincardi (2006), Active foreland deformation evidenced by shallow folds and faults affecting late Quaternary shelf-slope deposits (Adriatic Sea, Italy), *Basin Research*, *18*, 171–188, doi: 10.1111/j.1365-2117.2006.00289.x

Robertson, P.K. (1990), Soil Classification Using the Cone Penetration Test, *Canadian Geotechnical Journal*, *27*, 151-158.

Schultheiss, P.J., S.D. McPhail, A.R. Packwood, and B. Hart (1985), An instrument to measure differential pore pressures in deep ocean sediments: Pop-Up-Pore Pressure Instrument (PUPPI), Wormley, UK, Institute of Oceanographic Sciences, 57pp.

Skempton, A.W. (1954), Discussion of the structure of inorganic soils, *J. Soil Mech. Found Div.*, *80*, 263–264.

Sultan, N., P. Cochonat, M. Canals, A. Cattaneo, B. Dennielou, H. Haflidason, J.S. Laberg, D. Long, D., J. Mienert, F. Trincardi, R. Urgeles, T. Vorren, and C. Wilson (2004), Triggering Mechanisms of Slope Instability Processes and Sediment Failures On Continental Margins: A Geotechnical Approach, *Mar. Geol.*, *213*, 291– 321.

Terzaghi, K, and RB. Peck (1967), Soil mechanics in engineering practice, 2nd edn. Wiley, New York.

Tinti, S., and A. Armigliato (2003), The use of scenarios to evaluate the tsunami impact in southern Italy, *Mar. Geol.*, *199*, 221– 243.

Tinti, S., A. Maramai, and P. Favali (1995), The Gargano Promontory: an important Italian seismogenetic–tsunamigenic area, *Mar. Geol.*, *122*, 227– 241.

Trincardi, F., and W.R. Normark (1988), Sediment waves on the Tiber pro-delta slope, *Geo-Marine Lett.*, *8*, 149-157.

Trincardi, F., A. Cattaneo, A. Correggiari, and D. Ridente (2004), Evidence of soft-sediment deformation, fluid escape, sediment failure and regional weak layers within the late Quaternary mud deposits of the Adriatic Sea, *Mar. Geol.*, *213*, 91– 119.

Urgeles, R., et al. (2007). Sediment undulations on the Llobregat prodelta: Signs of early slope instability or sedimentary bedforms?, *J. Geophys. Res.*, *112*, B05102, doi:10.1029/2005JB003929.

Varnes, D.J. (1978), Slope movement types and processes. In: Schuster, R.L., Krizek, R.J. (Eds.), Landslides—Analysis and Control, Special Report 176. Transportation Research Board, Washington, D.C., pp. 12– 33.

Vigliotti, L., K.L. Verosub, A. Cattaneo, F. Trincardi, A. Asioli and A. Piva, A (2008). Palaeomagnetic and rock magnetic analysis of Holocene deposits from the Adriatic Sea: detecting and dating short- term fluctuations in sediment supply, *The Holocene*, *18*, 141-152.

Yang, Z., J. Lu, and A. Elgamal (2004), A Web-based Platform for Live Internet Computation of Seismic Ground Response, *Advances in Engineering Software*, *35*, 249-259.

APPENDIX A1 – SHEAR STRENGTH UNDER STATIC LOADING

The undrained shear strength, whether measured by torvane, fall cone or vane shear strength tests, shows consistent trends (Figure A 1). The torvane measurements were performed during the cruise shortly after the cores arrived aboard, whereas the fall cone and vane tests were conducted in the laboratory about 4 months after the cruise. This indicates that the cores suffered little dewatering and disturbance during the transport and storage process.

The undrained shear strength follows an almost linear increase profile with depth. Near the seafloor the undrained shear strength shows values of 5 to 6 kPa, whereas near the bottom of the borehole values range between 28 and 40 kPa. This linear trend is only disrupted at about 11mbsf where a sudden increase in shear strength is observed both in the Torvane and fall cone data and, in a more subdued way, in the vane tests. Such an increase divides the strength profile in an upper section (seafloor to 11 mbsf) where values increase from 5 to 13 kPa, and a lower section where undrained shear strength ranges from 25 to 40 kPa. The strength gradients are therefore similar in the upper and lower profile sections with a shift between 10 and 11 mbsf of about 12 kPa.

Static triaxial tests show that sediment from level 3 is characterized by a high internal friction angle corresponding to 36 degree (Figure A 2). The internal friction angle from the surrounding clayey sediment is 30 degree (Figure A 2).

APPENDIX A2 – SHEAR STRENGTH UNDER CYCLIC LOADING

Figure A 3 through Figure A 5 present three typical cyclic triaxial tests carried out on samples from the three different levels: the lower sandy layer (level 3 - Figure 4), the silty clay layer above the maximum flooding surface (level 2 - Figure 4) and the surrounding matrix clayey sediment in order to understand stratigraphic controls in the genesis of the observed features. For each cyclic test, three diagrams are presented showing:

- The applied cyclic shear stress versus the mean effective stress
- The applied cyclic shear stress versus the shear strain
- The excess pore pressure generated by the cyclic loading normalized with respect to the initial effective confining pressure (σ'_{30}) as a function of the number of cycles.

For sample S20 (Figure A 3), taken from a clayey layer (Table 1), the sediment was set to an effective confining pressure of 100 kPa and the applied cyclic shear stress was equal to 100 kPa. Cyclic softening failure occurred for sample S20 (shear strain greater than 20%) after 115 uniform cycles (Figure A 3). For sample S1 from hole PRAD2-6 (Figure A 4), obtained from the silty clay layer above the mfs (level 2), sediment was confined under an effective stress of 250 kPa and was loaded under an applied cyclic shear stress of 190 kPa. Liquefaction (excess pore pressure greater than 90 % of the initial effective confining pressure) occurred for S1 after 84 uniform cycles (Figure A 4). The last example shows the cyclic tests carried out on sample S40 (Table 1), recovered from the lower sandy layer (level 3). The sample was confined under an effective confining pressure of 350 kPa and cyclically loaded under a shear stress of 270 kPa. Liquefaction occurred for sample S40 after only 6 uniform cycles (Figure A 5).

Hole	Lat	Lon	Water depth (m)	Depth below seafloor (m)	Type
PRAD2-3	42°27'20.39"N	14°25'54.34"E	56.3	30.0	CPTU
PRAD2-5	42°27'20.21"N	14°25'54.08"E	56.3	32.8	Cores
PRAD2-6	42°27'20.23"N	14°25'54.32"E	56.3	18.0	CPTU
PRAD2-6	42°27'20.23"N	14°25'54.32"E	56.3	19.8→21.3	Cores

Table 1. Location, water depth and depth below seafloor of the different geotechnical boreholes from the Adriatic site and considered in this work.

Hole	Sample	Depth (top of the sample: mbsf)
PRAD2-5	S3	02.45
PRAD2-5	S8	06.45
PRAD2-5	S10	08.05
PRAD2-5	S13	10.45
PRAD2-5	S18	14.40
PRAD2-5	S19	15.25
PRAD2-5	S20	16.05
PRAD2-5	S23	17.90
PRAD2-5	S26	20.85
PRAD2-5	S29	23.25
PRAD2-5	S31	24.85
PRAD2-5	S36	28.85
PRAD2-5	S38	30.45
PRAD2-5	S40	32.05
PRAD2-6	S1	20.85

Table 2. Depth below seafloor of the different samples tested in laboratory in the present work.

Hole	Sample	Depth (mbsf)	$\sigma_{d,cyc}$ (kPa)	σ'_{30} (kPa)	CSR	Cycles to liquefaction or cyclic softening failure
PRAD2-5	s8	06.45	50	50	0.50	No failure/liquefaction
PRAD2-5	s10	08.05	30	65	0.23	No failure/liquefaction
PRAD2-5	s13	10.45	50	75	0.33	No failure/liquefaction
PRAD2-5	s20	16.05	100	100	0.50	116
PRAD2-5	s26	20.85	145	165	0.44	10
PRAD2-5	s26	20.85	80	165	0.24	No failure/liquefaction
PRAD2-5	s29	23.25	130	185	0.35	200
PRAD2-5	s31	24.85	150	250	0.30	No failure/liquefaction
PRAD2-5	s36	28.85	145	250	0.29	170
PRAD2-5	s38	30.45	245	350	0.35	10
PRAD2-5	s40	32.05	270	350	0.38	7
PRAD2-5	s40	32.05	300	350	0.43	5
PRAD2-6	s1	20.85	190	250	0.38	82
PRAD2-6	s1	20.85	175	250	0.35	100
PRAD2-6	s1	20.85	150	250	0.3	200

Table 3. Summary of the cyclic tests carried out on samples from the PRAD2-5 and PRAD2-6 sites.

Date	Time	Latitude	Longitude	Depth (km)	Magnitude	Distance (km)
02.07.2001	10 :04 :42.02	41.946	15.293	10	4.2	88.04

Table 4. Location and magnitude of the event of 2nd July 2001

Layer N°	Depth (m)	Type	Shear wave velocity (m/s)	Friction angle (degree) or Undrained shear strength (kPa)	Submerged unit weight (kN/m^3)
1	0.0→5.5	Cohesive soft	80	Su = 10	7.5
2	5.5→6.0	Cohesionless loose silt	140	φ = 30	8.0
3	6.0→19.5	Cohesive medium	100	Su = 20	8.5
4	19.5→20.5	Cohesionless loose silt	165	φ = 30	8.5
5	20.5→26.0	Cohesive medium	150	Su = 30	9.0
5	26.0→40.0	Cohesionless medium silt	200	φ = 36	10.0

Table 5. Mechanical parameters used in the Cyclic1D software to study the effect of an earthquake on the sedimentary behavior from the PRAD2 site.

NOTATION

Symbol	Definition
α	Effective cone section ratio
B_q	Pore pressure parameter
c'	Effective cohesion
CSR	Cyclic Stress Ratio
CRR	Cyclic Resistance Ratio
C_v	Hydraulic diffusivity
Δu	Excess pore pressure
e	Void ratio
Fr	Normalized friction ratio
fs	Sleeve friction
φ	Internal friction angle
g	Gravitational acceleration
G	Shear modulus
γ_w	Water unit weight
k	Permeability coefficient
OCR	Over-Consolidation ratio
PGA	Peak Ground Acceleration
PI	Plasticity Index
qc	Tip resistance
q_{net}	Net cone resistance
q_t	Corrected cone resistance
Q_t	Normalized cone resistance
Su	Undrained shear strength
σ_v	Vertical total stress
σ'_v	Vertical effective stress
σ'_{30}	Effective confining pressure
$\sigma_{d,cyc}$	Cyclic deviator stress
u_0	Hydrostatic pressure
u_2	Pore pressure measured immediately behind the cone
u_i	Hydrostatic pore pressure at the borehole base
V_p	Compressional wave velocity
V_s	Shear wave velocity

Figure 1. a) Location of PRAD2 site and thickness map in TWTT (ms) of the late Holocene mud wedge (from Cattaneo et al. 2004 and Trincardi et al. 2004) and b) stratigraphy at the site PRAD2 showing seafloor and subsurface irregularities (ISMAR data).

Figure 2. a) Corrected cone resistance q_t versus depth below seafloor. b) Unit sleeve friction resistance *fs* vs depth. c) Pore pressure u_2 vs depth (a, b, c and d from boreholes PRAD2-3 (15-32 mbsf) and PRAD2-6 (0-15 mbsf)). d) Unit weight from γ-density compared to the unit weight determined from the water content values (PRAD2-5). e) Compressional wave velocity V_p versus depth from PRAD2-5. The sudden decrease of the V_p below 21 mbsf is probably related to gas exsolution.

Figure 3. Between 20.2 m and 20.9 m below seafloor, the CPTU measurements from borehole PRAD2-3 have detected the existence of a layer characterized by a relatively high cone resistance (a). a relatively high friction (b) and a decrease of the excess pore pressure (c). These in-situ measurements confirm what was observed in laboratory concerning the existence of a silty layer at this depth.

Figure 4. Data from PRAD2-5 hole: a) Unit weight b) grain size distribution c) P wave velocity d) water content e) plasticity index and f) liquidity index versus depth.

Figure 5. Correlation between geophysical data (seismic profile) and geotechnical properties

Figure 6. Potential liquefaction diagram: Cyclic resistance ratio as a function of the cycles to liquefaction

Figure 7. Overconsolidation ratio obtained from the oedometer tests and derived from the Undrained shear strength and the plasticity index (Skempton's equation).

Figure 8. a) Excess pore pressure versus depth derived from oedometer tests and calculation (SeCo software) using two different sedimentation rates (10 $m.ky^{-1}$ and 5 $m.kyr^{-1}$) b) void ratio versus vertical effective stress obtained from 9 different sediment samples and c) permeability versus void ratio obtained from 9 different samples and at different vertical effective stress. The SeCO software used the theoretical compressibility curve shown in figure-b and the theoretical permeability curve shown in figure-c.

Figure 9. Historical seismicity map of the study area during the last 400 years, b) Distance from epicenter to the study area of the main earthquakes from the last 400 years and d) Peak Ground Acceleration derived using the Idriss (1993) relationship. The magnitude and the *PGA* generated by the moderate 2001 earthquake are added to both diagrams.

Figure 10. a) Horizontal acceleration time history obtained from OFOS [*Mienert et al.*, 2002] and the final profile of b) excess pore pressure, c) vertical effective stress and d) CSR. CRR values obtained from the cyclic trixial tests for level 2 and level 3 (as defined in Figure 4-b) are added to figure 10-d.

Figure 11. Excess pore pressure profile for three different position of the silty clay layer (level 2 - Figure 4) a) at 10.5 mbsf b) at 5.5 mbsf and c) at 3 mbsf.

Figure A 1. Undrained shear strength *Su* acquired from PRAD2-5 using a) Torvane b) Fall cone and c) Shear Vane. A limit at around 10 mbsf corresponding to an increase of the undrained shear strength was identified from the torvane and the fall cone.

Figure A 2. static triaxial tests : Stress paths in the shear stress -mean effective stress diagram.

Figure A 3. Undrained cyclic triaxial test: PRAD2-5 – S20 (clayey layer – 16.05 mbsf).

Figure A 4. Undrained cyclic triaxial test: PRAD2-6 – S21 (silty clay layer – 20.85 mbsf).

Figure A 5. Undrained cyclic triaxial test: PRAD2-5 – S40 (sandy layer – 32.05 mbsf).

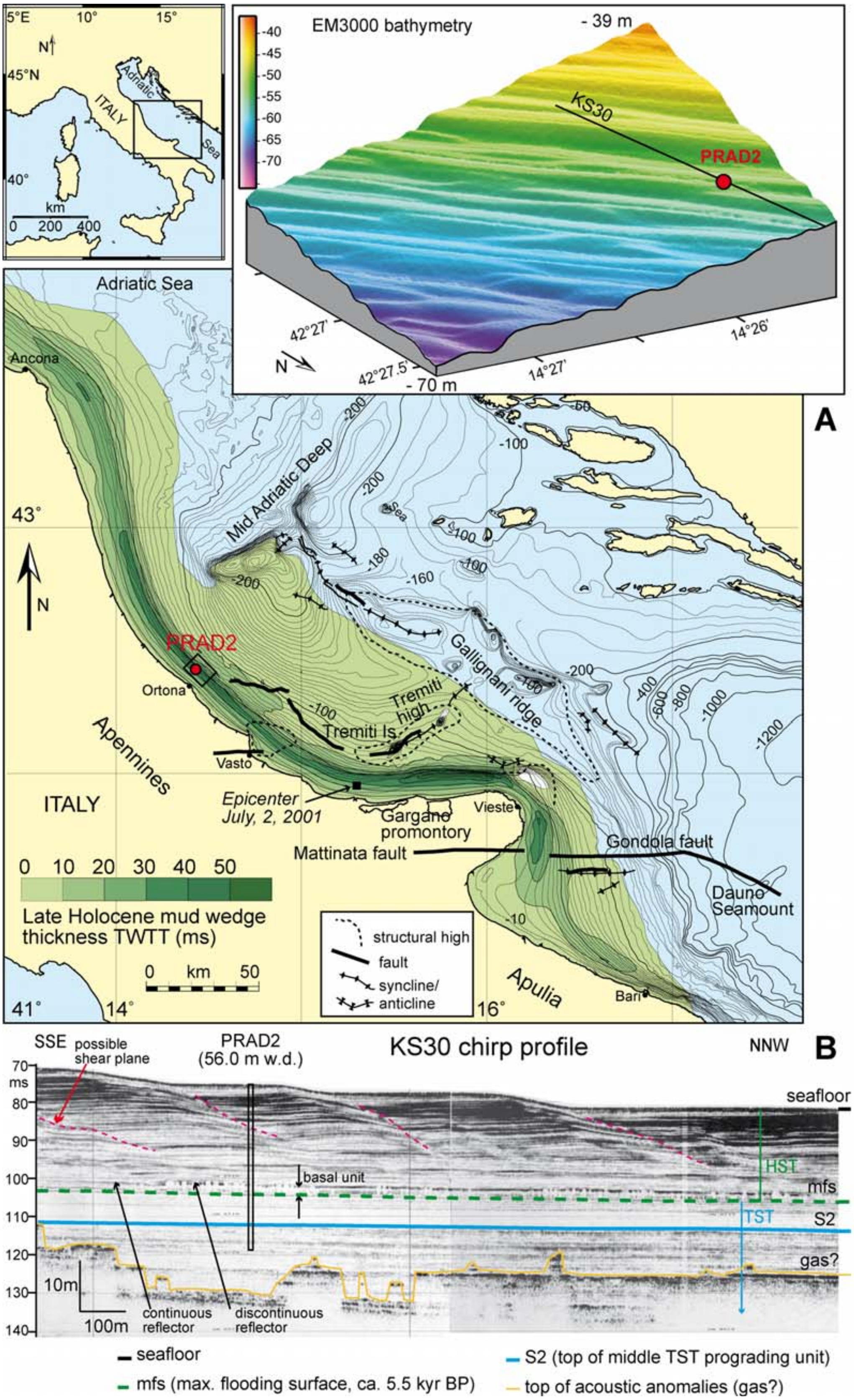

EM3000 bathymetry
- 39 m
KS30
PRAD2
N
42°27'
42°27.5'
- 70 m
14°27'
14°26'
5°E
10°
15°
45°N
40°
ITALY
Adriatic
Sea
km
0 200 400
Adriatic Sea
Ancona
A
43°
Mid Adriatic Deep
N
PRAD2
Ortona
Apennines
Tremiti high
Tremiti Is.
Galligani ridge
Vasto
ITALY
Epicenter
July, 2, 2001
Gargano promontory
Vieste
Mattinata fault
Gondola fault
Dauno Seamount
0 10 20 30 40 50
Late Holocene mud wedge thickness TWTT (ms)
0 km 50
structural high
fault
syncline/
anticline
Apulia
Bari
41°
14°
16°
SSE
possible shear plane
PRAD2
(56.0 m w.d.)
KS30 chirp profile
NNW
B
seafloor
HST
mfs
TST
S2
gas?
basal unit
10m
100m
continuous reflector
discontinuous reflector
seafloor
mfs (max. flooding surface, ca. 5.5 kyr BP)
S2 (top of middle TST prograding unit)
top of acoustic anomalies (gas?)

Figure 1.

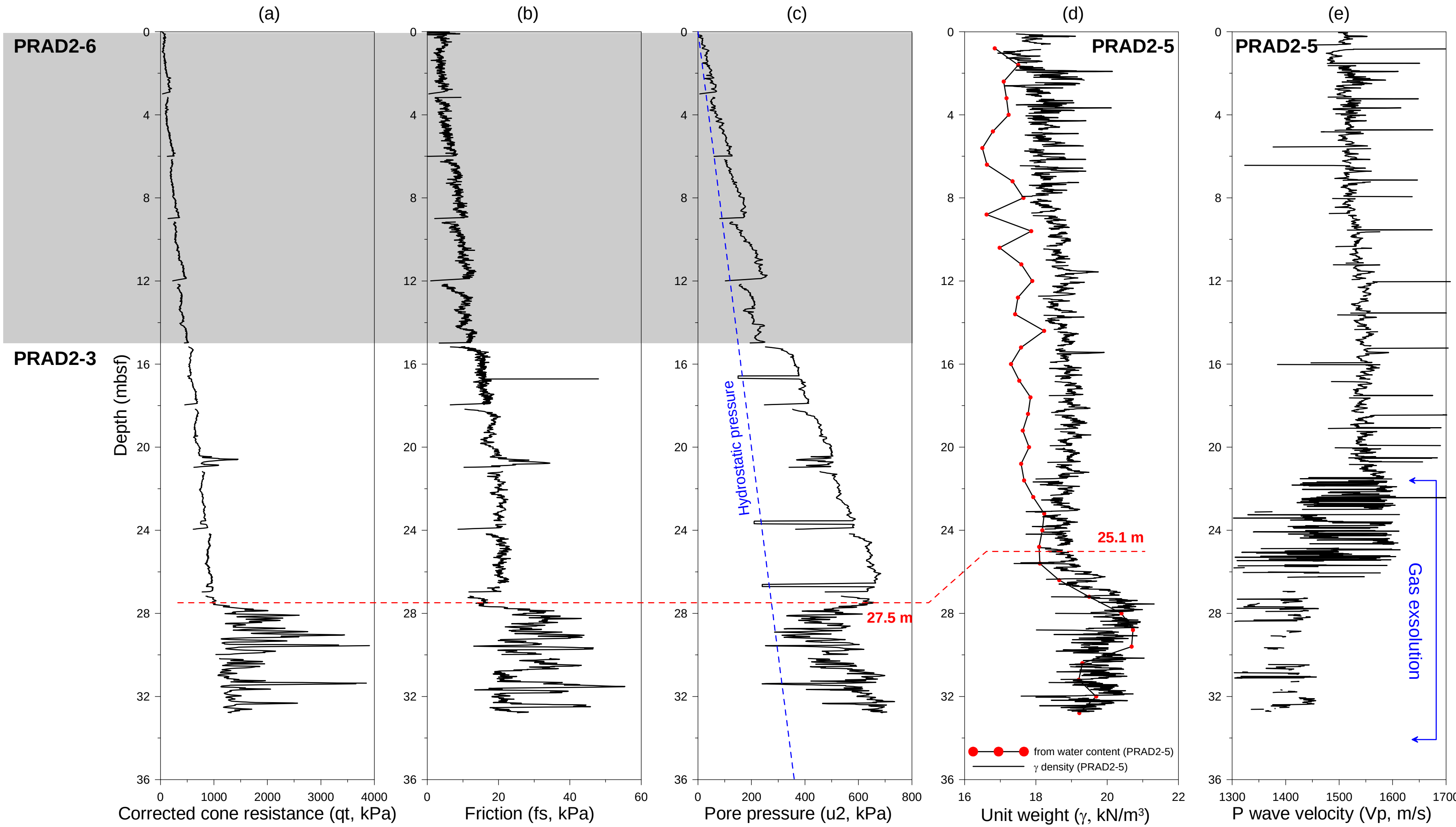

(a)
(b)
(c)
(d)
(e)
PRAD2-6
PRAD2-3
PRAD2-5
PRAD2-5
Depth (mbsf)
Hydrostatic pressure
27.5 m
25.1 m
Gas exsolution
from water content (PRAD2-5)
γ density (PRAD2-5)
Corrected cone resistance (qt, kPa)
Friction (fs, kPa)
Pore pressure (u2, kPa)
Unit weight (γ, kN/m³)
P wave velocity (Vp, m/s)

Figure 2.

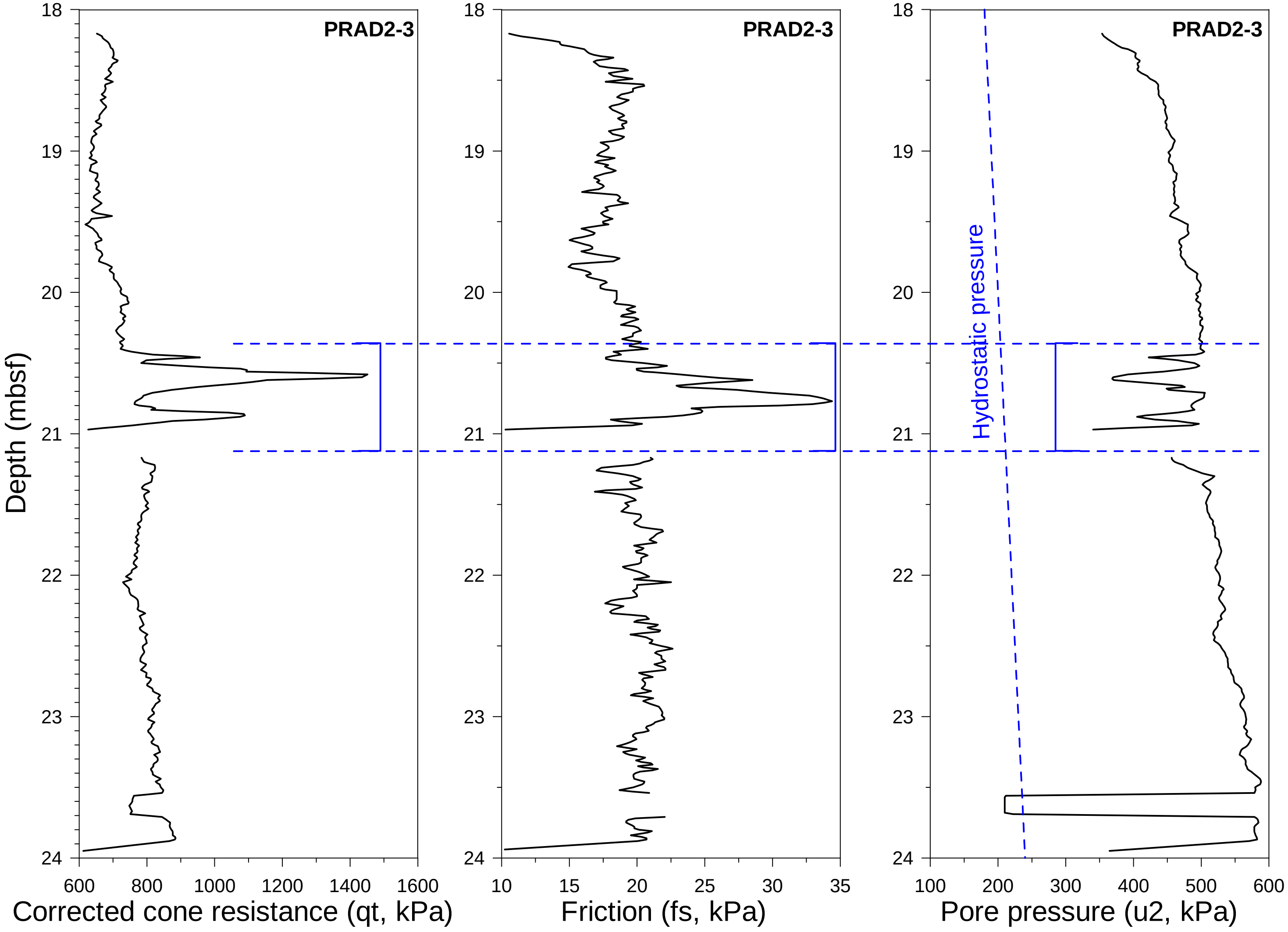

PRAD2-3
PRAD2-3
PRAD2-3
Depth (mbsf)
Hydrostatic pressure
18
19
20
21
22
23
24
600
800
1000
1200
1400
1600
Corrected cone resistance (qt, kPa)
10
15
20
25
30
35
Friction (fs, kPa)
100
200
300
400
500
600
Pore pressure (u2, kPa)

Figure 3.

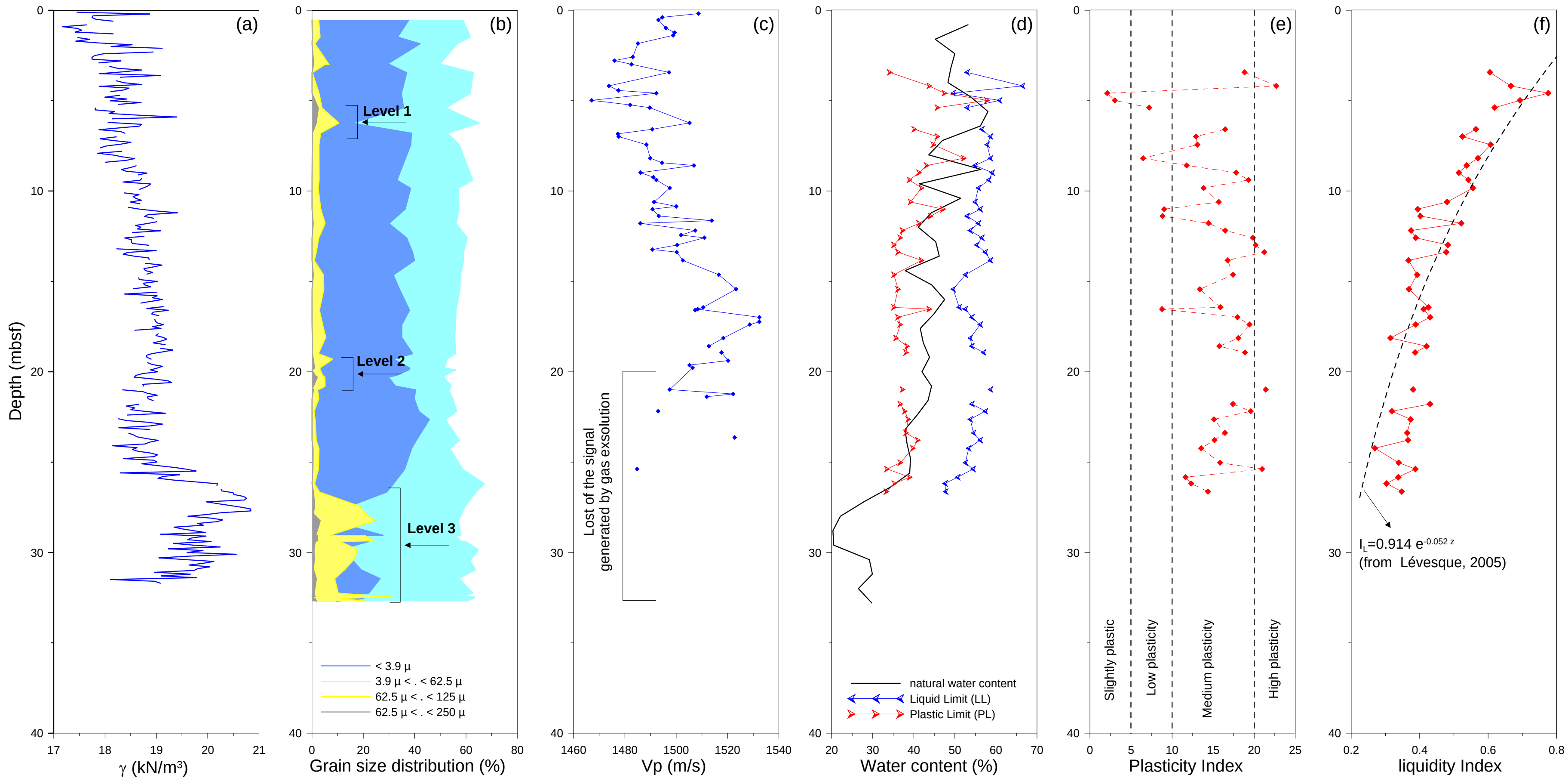

(a)
(b)
(c)
(d)
(e)
(f)
Depth (mbsf)
γ (kN/m³)
Grain size distribution (%)
Vp (m/s)
Water content (%)
Plasticity Index
liquidity Index
Level 1
Level 2
Level 3
< 3.9 µ
3.9 µ < . < 62.5 µ
62.5 µ < . < 125 µ
62.5 µ < . < 250 µ
Lost of the signal generated by gas exsolution
natural water content
Liquid Limit (LL)
Plastic Limit (PL)
Slightly plastic
Low plasticity
Medium plasticity
High plasticity
I_L=0.914 $e^{-0.052 z}$
(from Lévesque, 2005)

Figure 4.

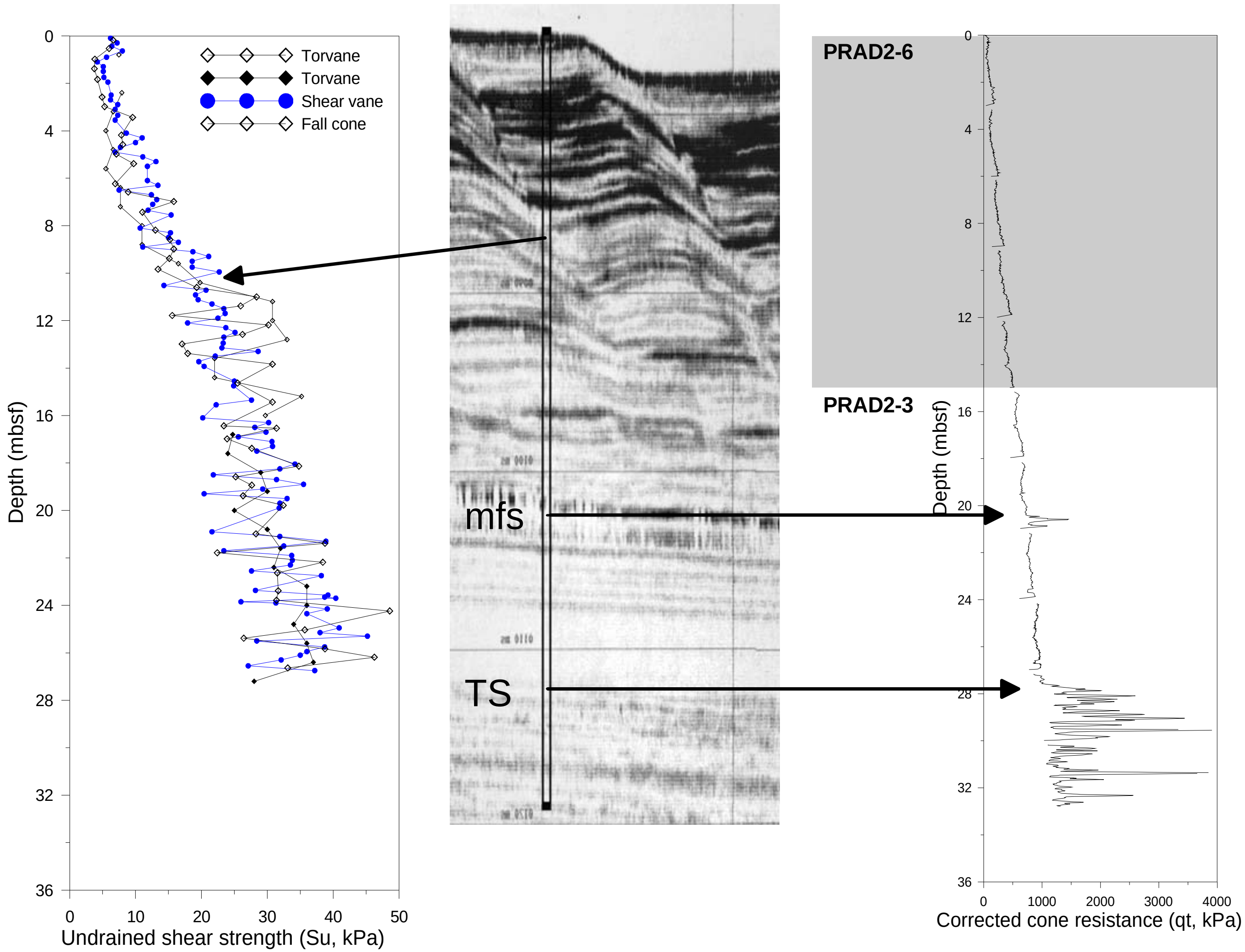
Torvane
Torvane
Shear vane
Fall cone
Depth (mbsf)
Undrained shear strength (Su, kPa)
0
4
8
12
16
20
24
28
32
36
0
10
20
30
40
50
mfs
TS
PRAD2-6
PRAD2-3
Depth (mbsf)
0
1000
2000
3000
4000
Corrected cone resistance (qt, kPa)

Figure 5.

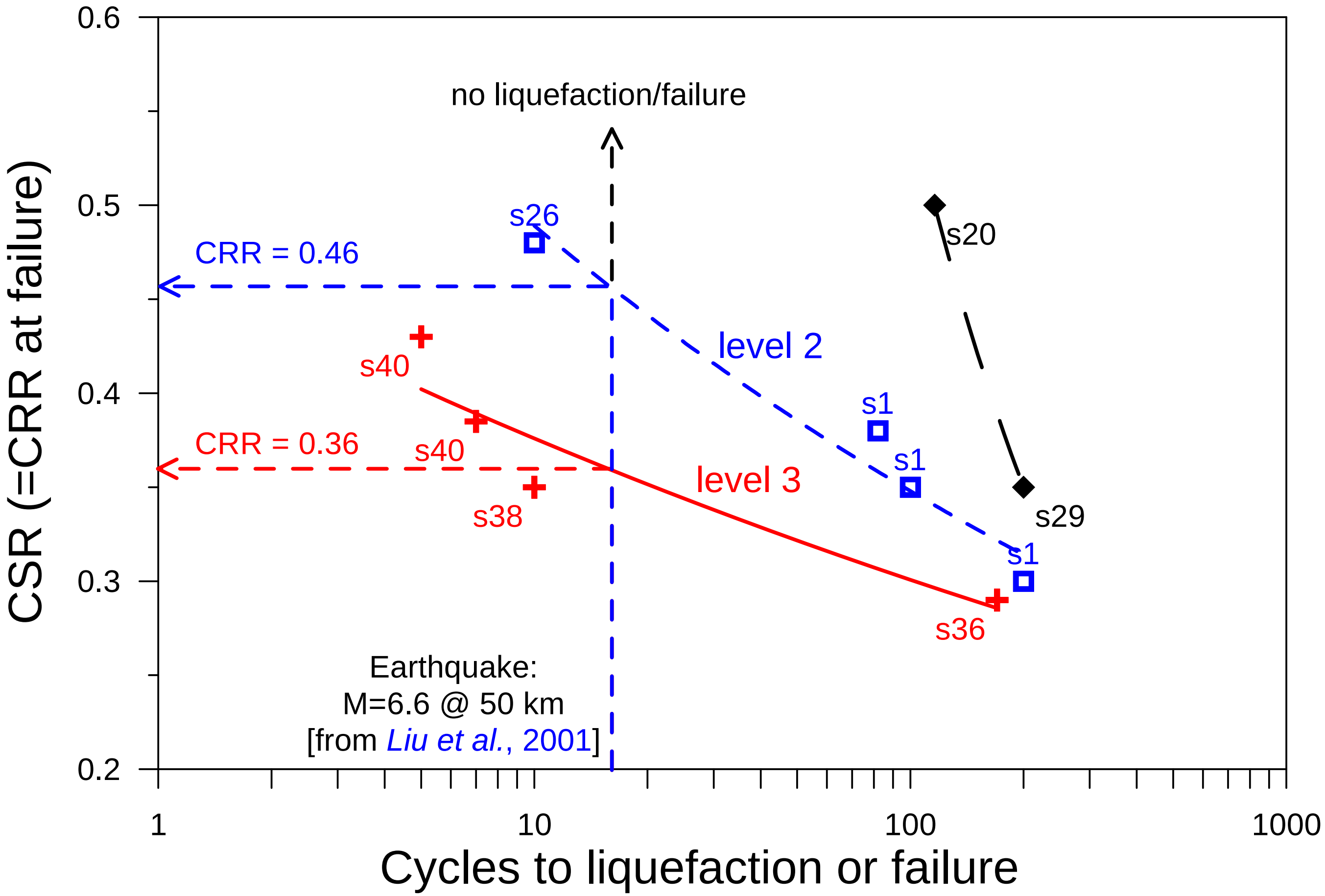

0.6
0.5
0.4
0.3
0.2
CSR (=CRR at failure)
no liquefaction/failure
CRR = 0.46
CRR = 0.36
s26
s20
level 2
s40
s40
s1
s1
level 3
s38
s29
s1
s36
Earthquake:
M=6.6 @ 50 km
[from Liu et al., 2001]
1
10
100
1000
Cycles to liquefaction or failure

Figure 6.

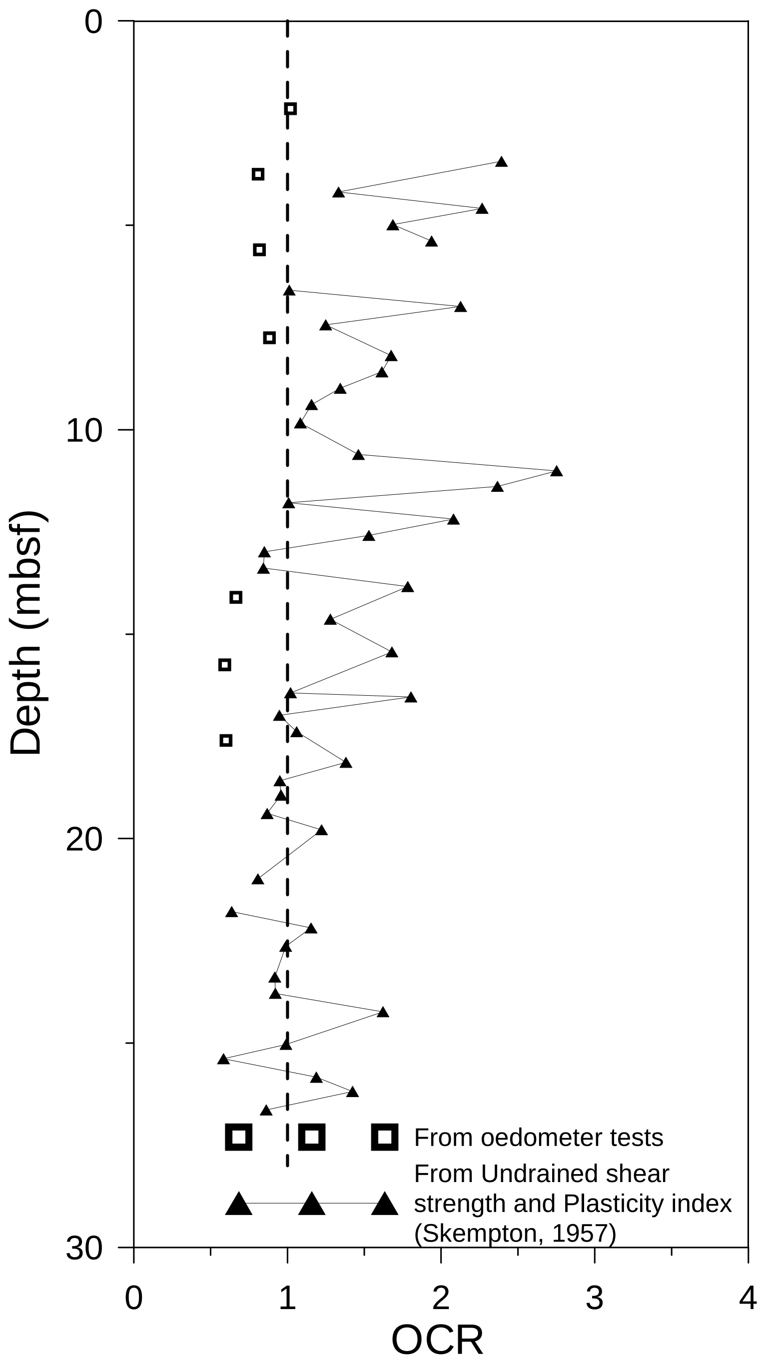
0
10
20
30
Depth (mbsf)
0
1
2
3
4
OCR
From oedometer tests
From Undrained shear strength and Plasticity index (Skempton, 1957)

Figure 7.

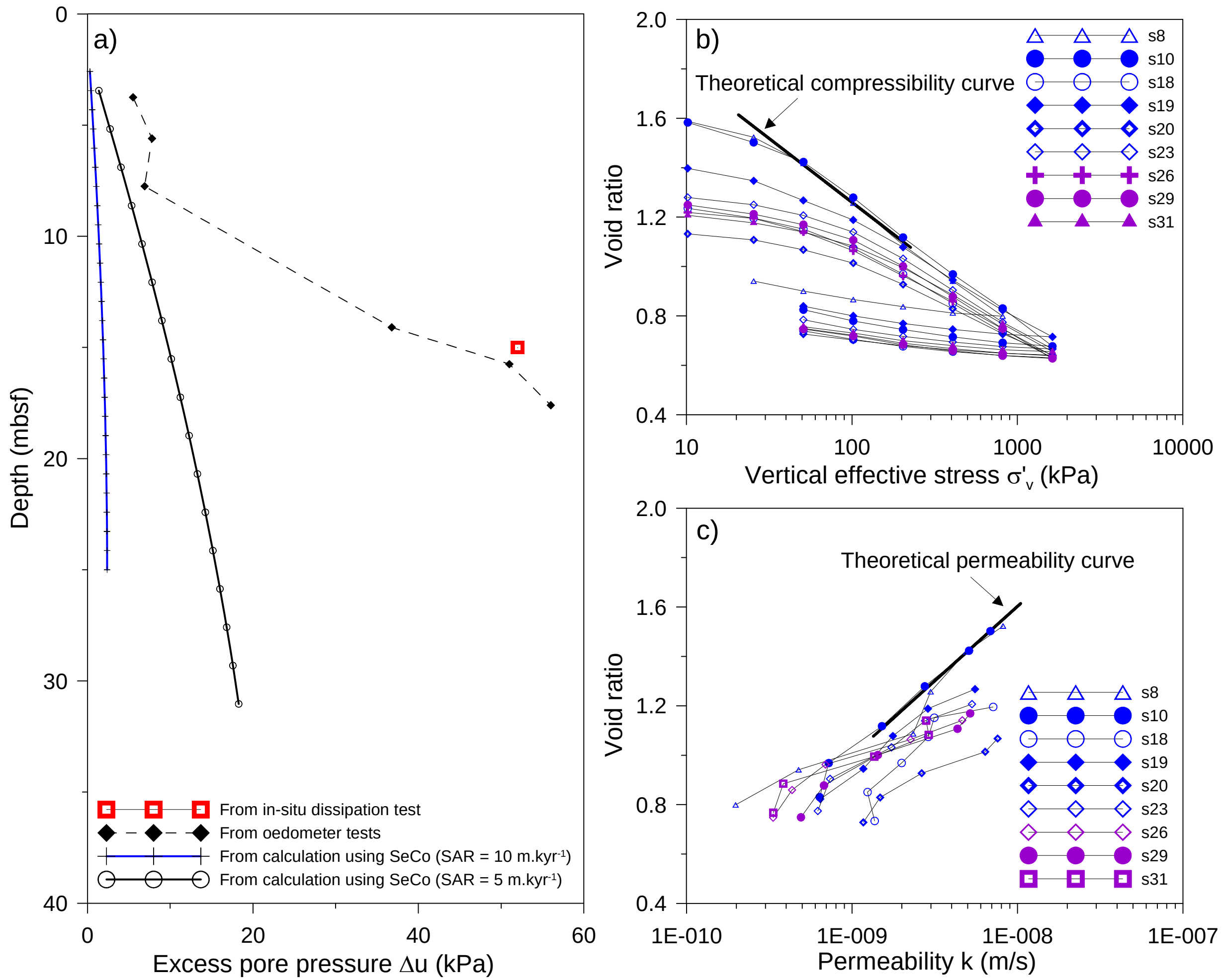

a)
Depth (mbsf)
Excess pore pressure Δu (kPa)
From in-situ dissipation test
From oedometer tests
From calculation using SeCo (SAR = 10 m.kyr-1)
From calculation using SeCo (SAR = 5 m.kyr-1)
b)
Theoretical compressibility curve
Void ratio
Vertical effective stress σ'v (kPa)
s8
s10
s18
s19
s20
s23
s26
s29
s31
c)
Theoretical permeability curve
Void ratio
Permeability k (m/s)
s8
s10
s18
s19
s20
s23
s26
s29
s31

Figure 8.

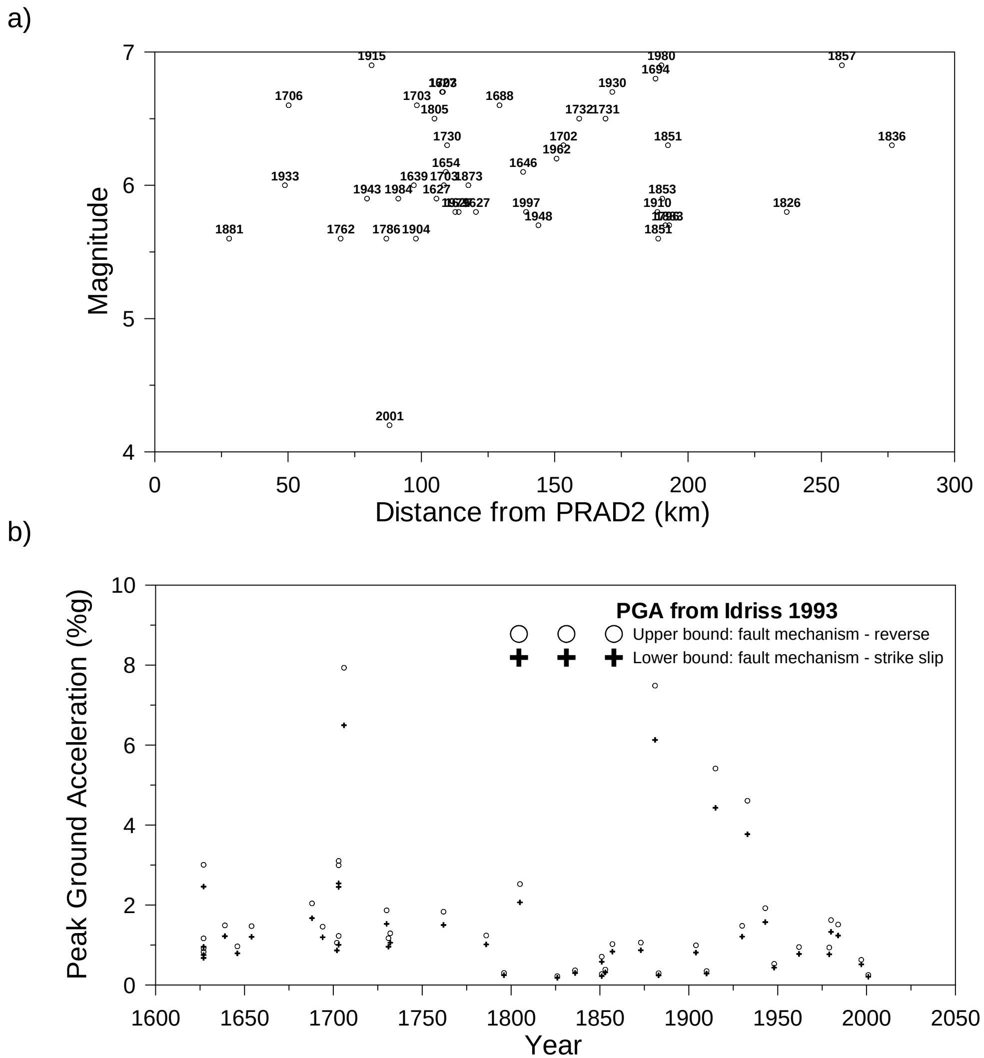
a)
Magnitude
Distance from PRAD2 (km)
b)
Peak Ground Acceleration (%g)
Year
PGA from Idriss 1993
Upper bound: fault mechanism - reverse
Lower bound: fault mechanism - strike slip

Figure 9.

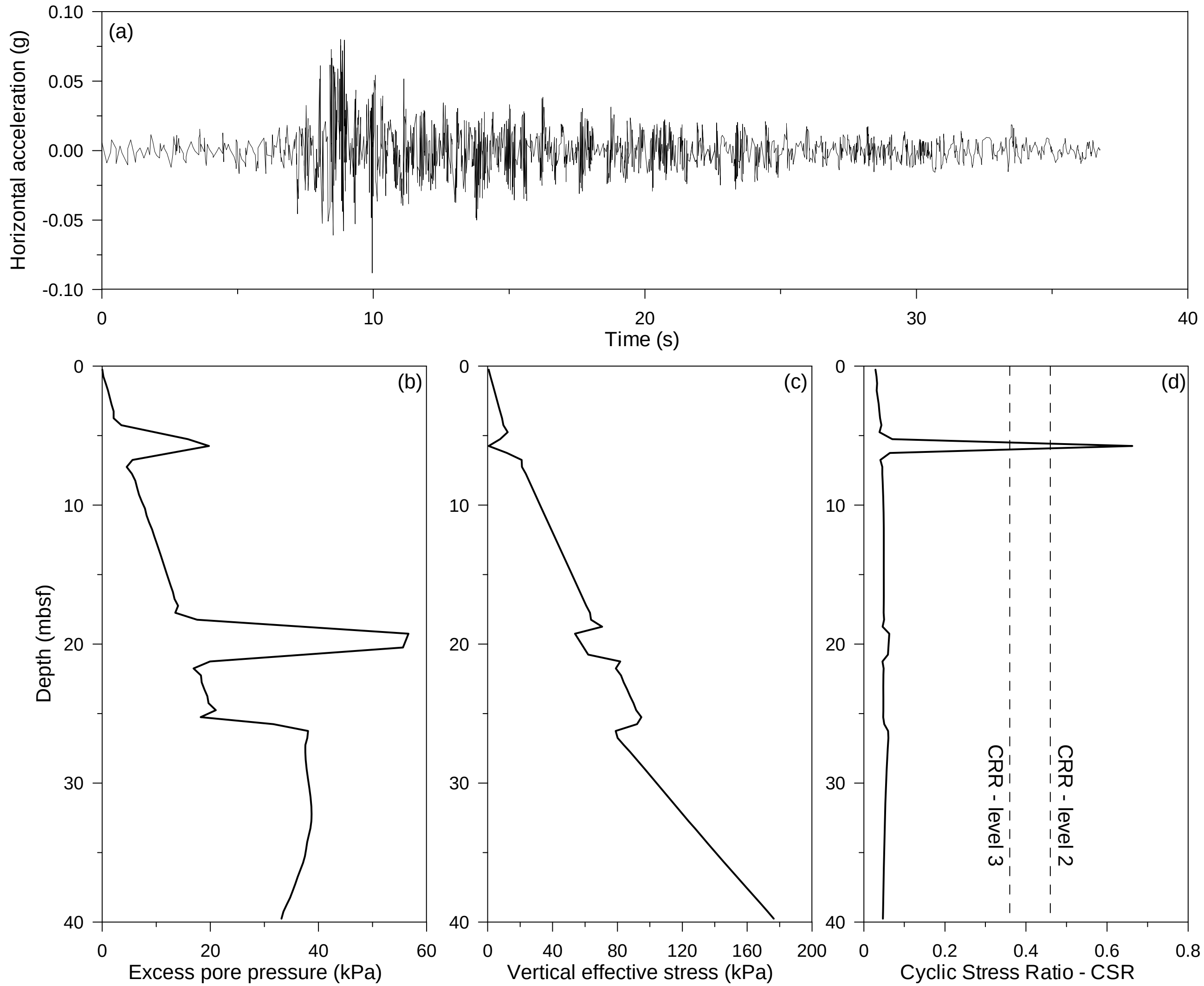
(a)
Horizontal acceleration (g)
0.10
0.05
0.00
-0.05
-0.10
0
10
20
30
40
Time (s)
(b)
(c)
(d)
Depth (mbsf)
0
10
20
30
40
Excess pore pressure (kPa)
Vertical effective stress (kPa)
Cyclic Stress Ratio - CSR
CRR - level 3
CRR - level 2

Figure 10.

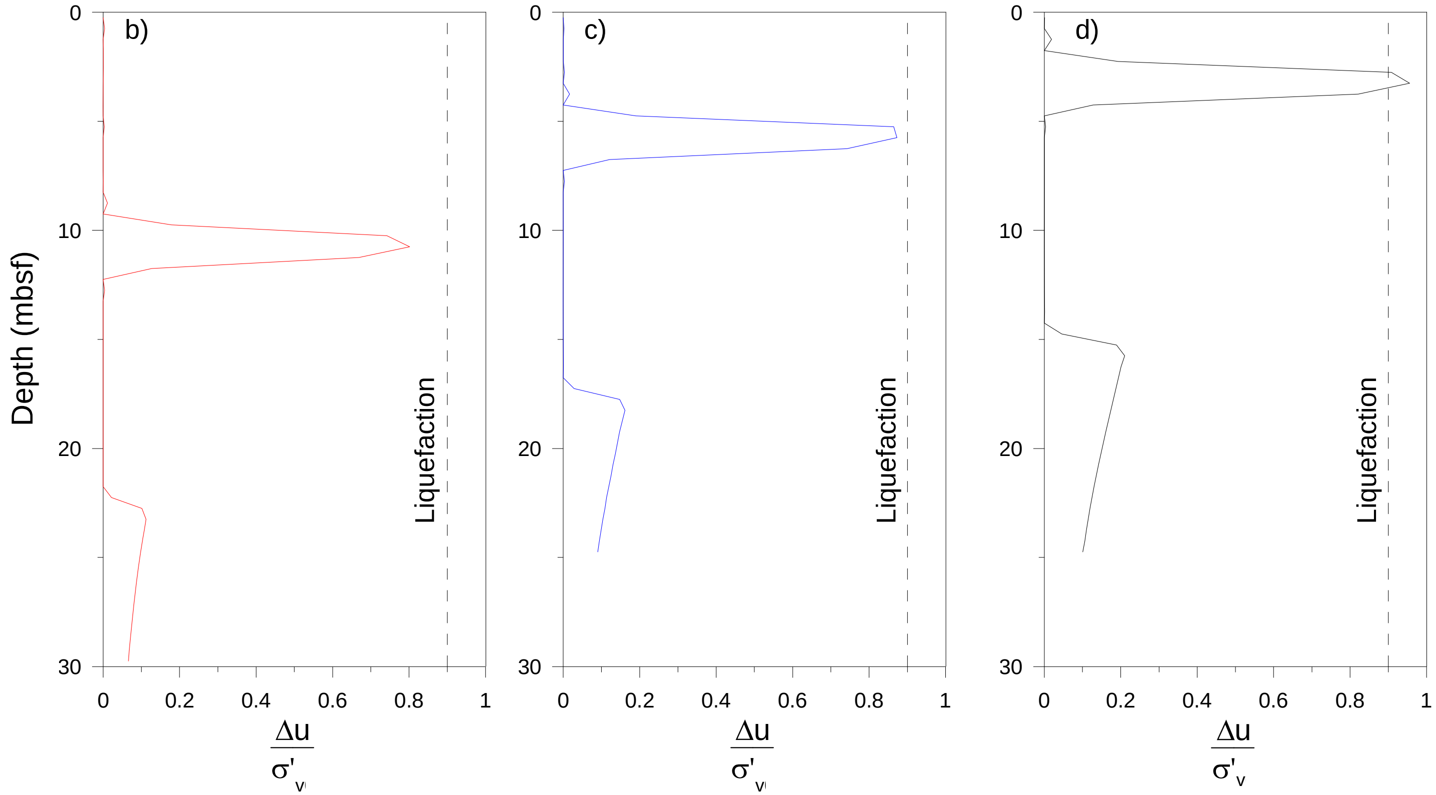

Figure 11.

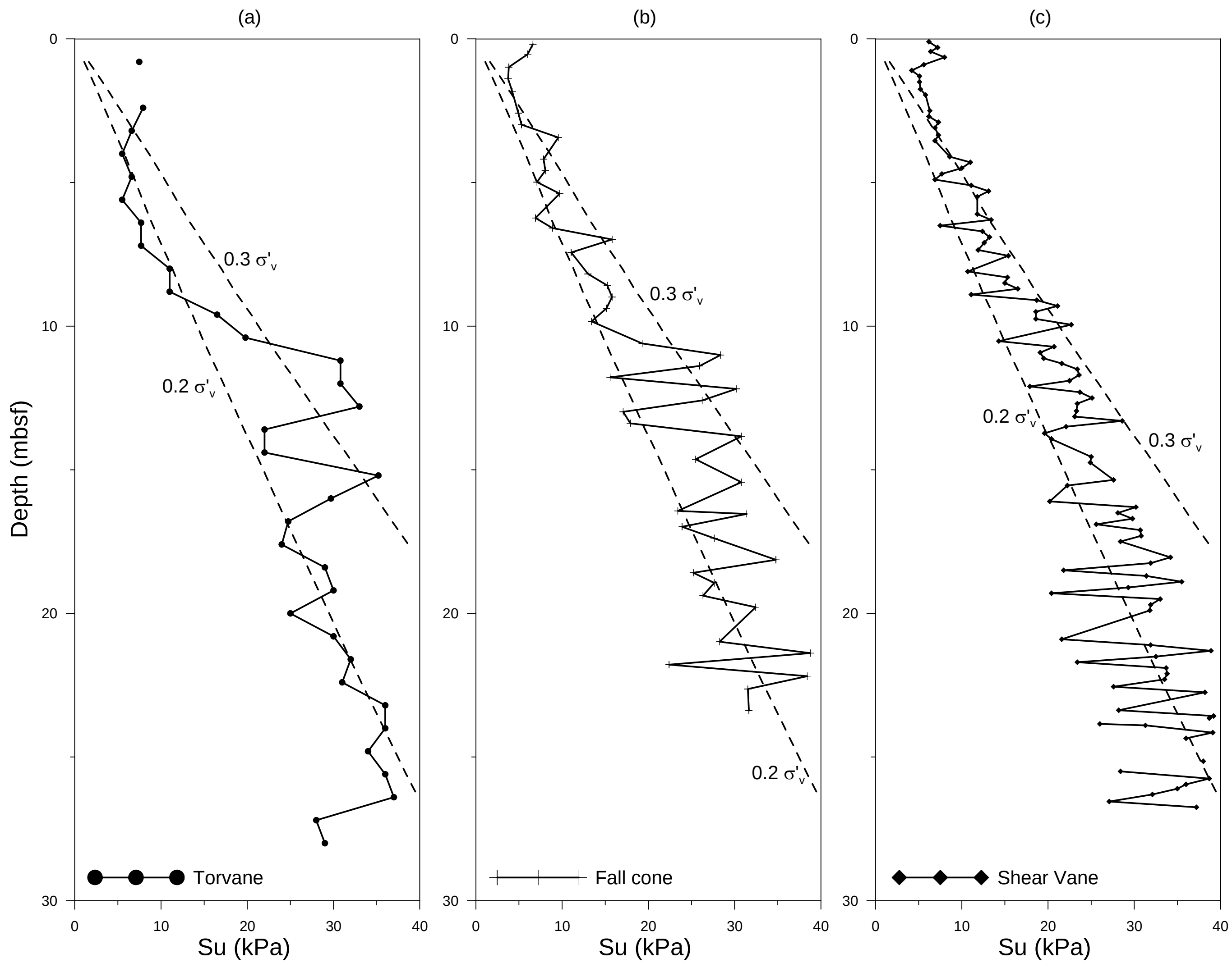

(a)
(b)
(c)
Depth (mbsf)
Su (kPa)
Su (kPa)
Su (kPa)
0.3 σ'v
0.2 σ'v
0.3 σ'v
0.2 σ'v
0.2 σ'v
0.3 σ'v
Torvane
Fall cone
Shear Vane
0
10
20
30
0
10
20
30
40

Figure A1.

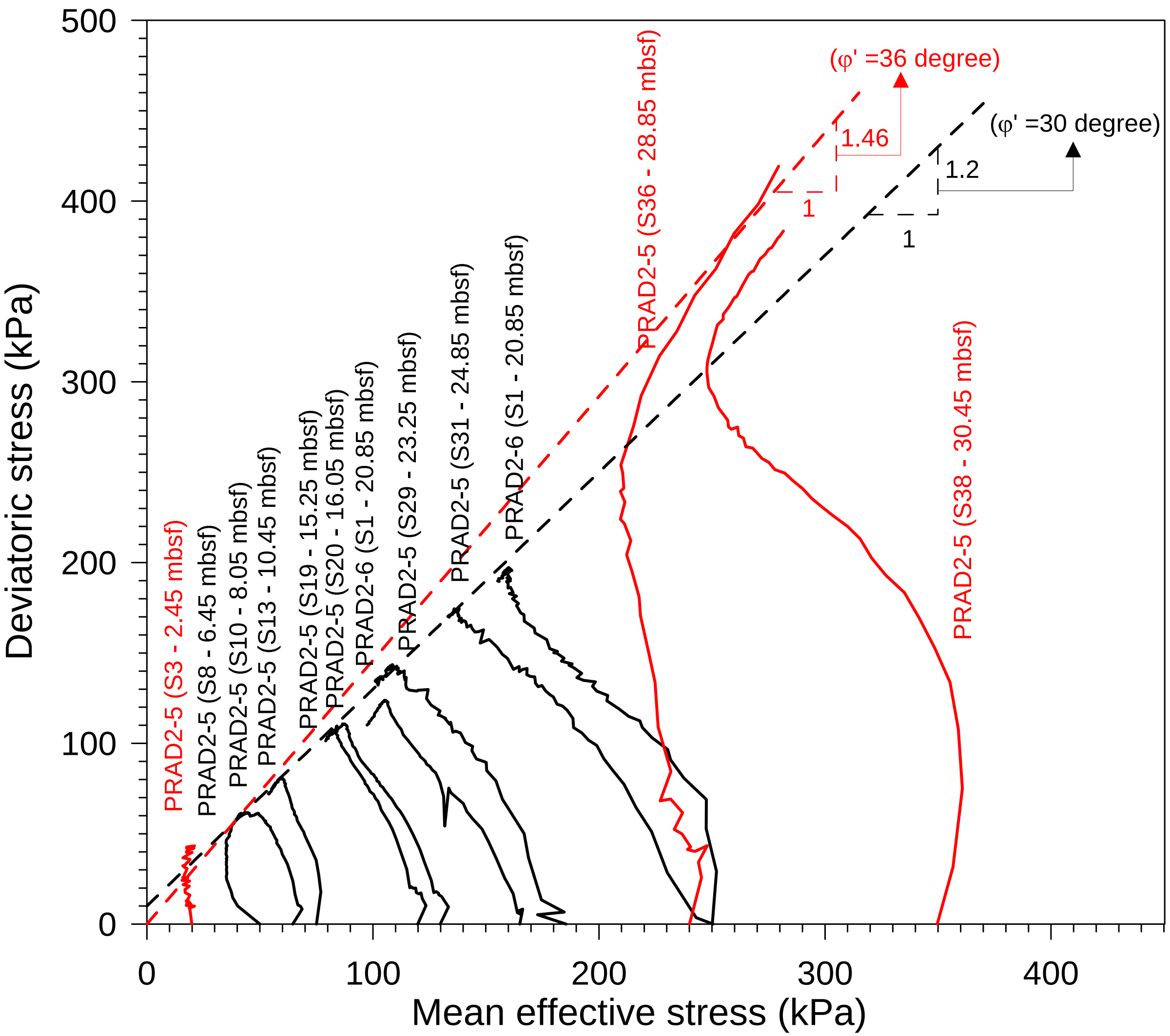

Deviatoric stress (kPa)
Mean effective stress (kPa)
500
400
300
200
100
0
0
100
200
300
400
(φ' =36 degree)
(φ' =30 degree)
1.46
1
1.2
1
PRAD2-5 (S3 - 2.45 mbsf)
PRAD2-5 (S8 - 6.45 mbsf)
PRAD2-5 (S10 - 8.05 mbsf)
PRAD2-5 (S13 - 10.45 mbsf)
PRAD2-5 (S19 - 15.25 mbsf)
PRAD2-5 (S20 - 16.05 mbsf)
PRAD2-6 (S1 - 20.85 mbsf)
PRAD2-5 (S29 - 23.25 mbsf)
PRAD2-5 (S31 - 24.85 mbsf)
PRAD2-6 (S1 - 20.85 mbsf)
PRAD2-5 (S36 - 28.85 mbsf)
PRAD2-5 (S38 - 30.45 mbsf)

Figure A2.

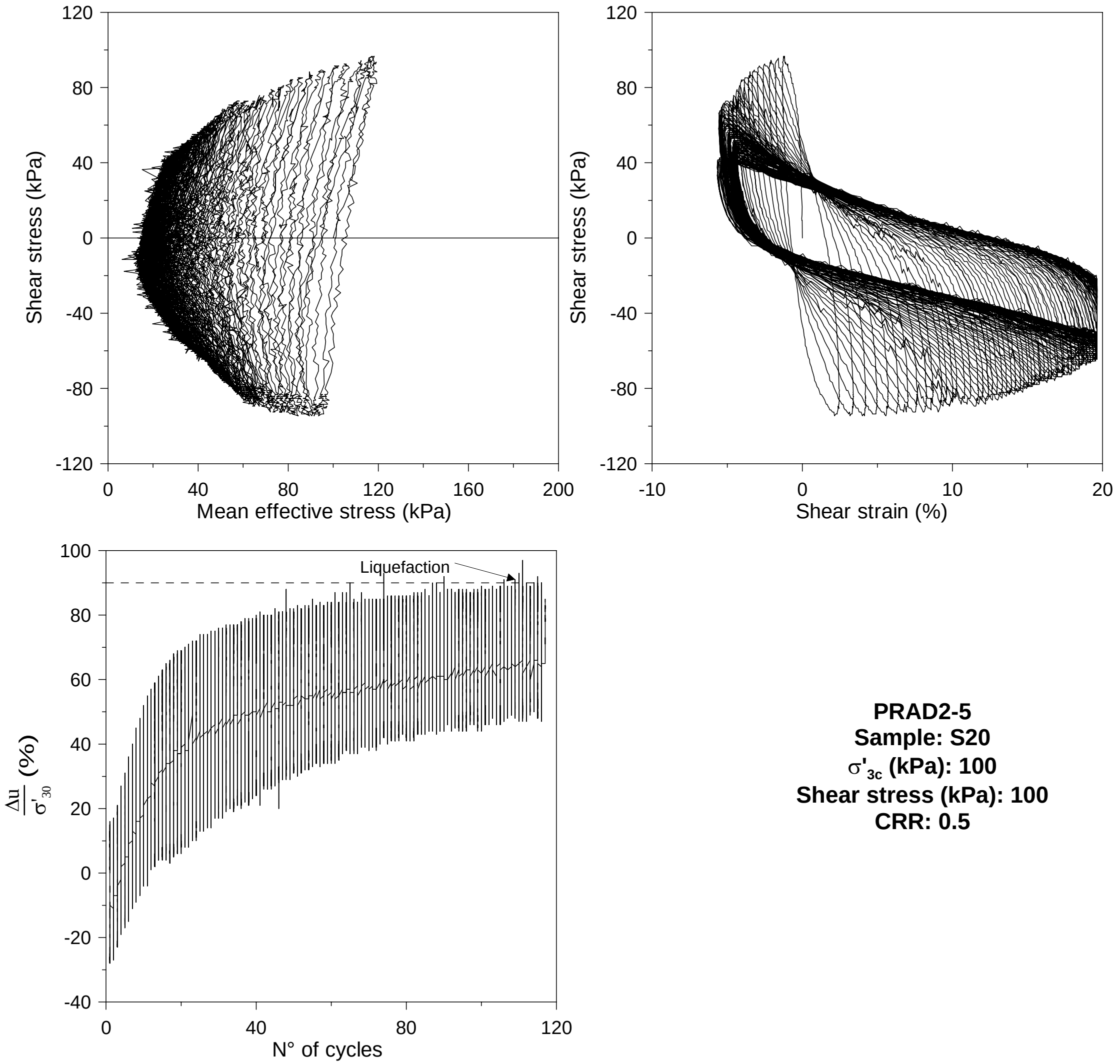
Shear stress (kPa)
Mean effective stress (kPa)
Shear strain (%)
Liquefaction
Δu/σ'30 (%)
N° of cycles
PRAD2-5
Sample: S20
σ'3c (kPa): 100
Shear stress (kPa): 100
CRR: 0.5

Figure A3.

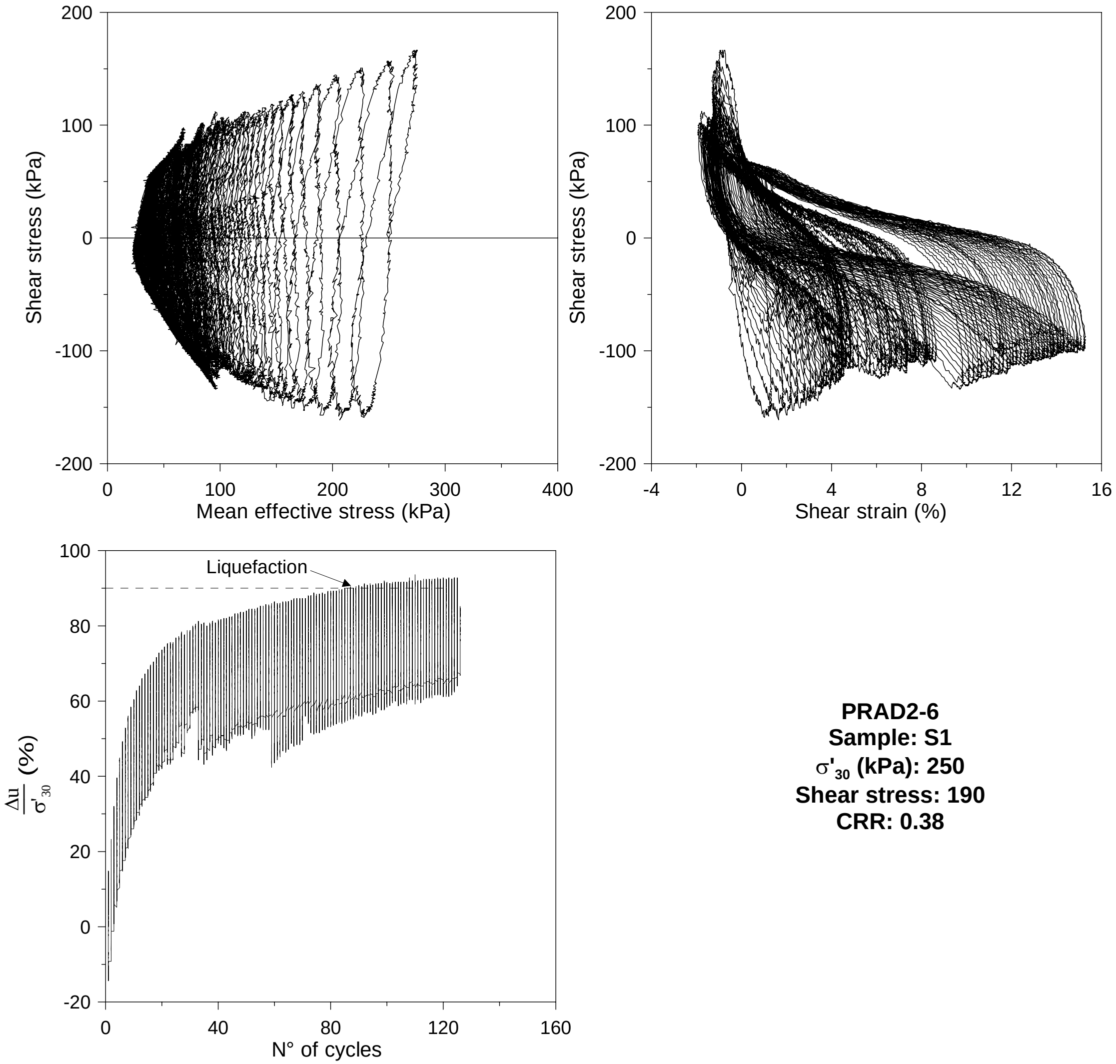
Shear stress (kPa)
Mean effective stress (kPa)
Shear stress (kPa)
Shear strain (%)
Liquefaction
$\frac{\Delta u}{\sigma'_{30}}$ (%)
N° of cycles
PRAD2-6
Sample: S1
σ'_{30} (kPa): 250
Shear stress: 190
CRR: 0.38

Figure A4.

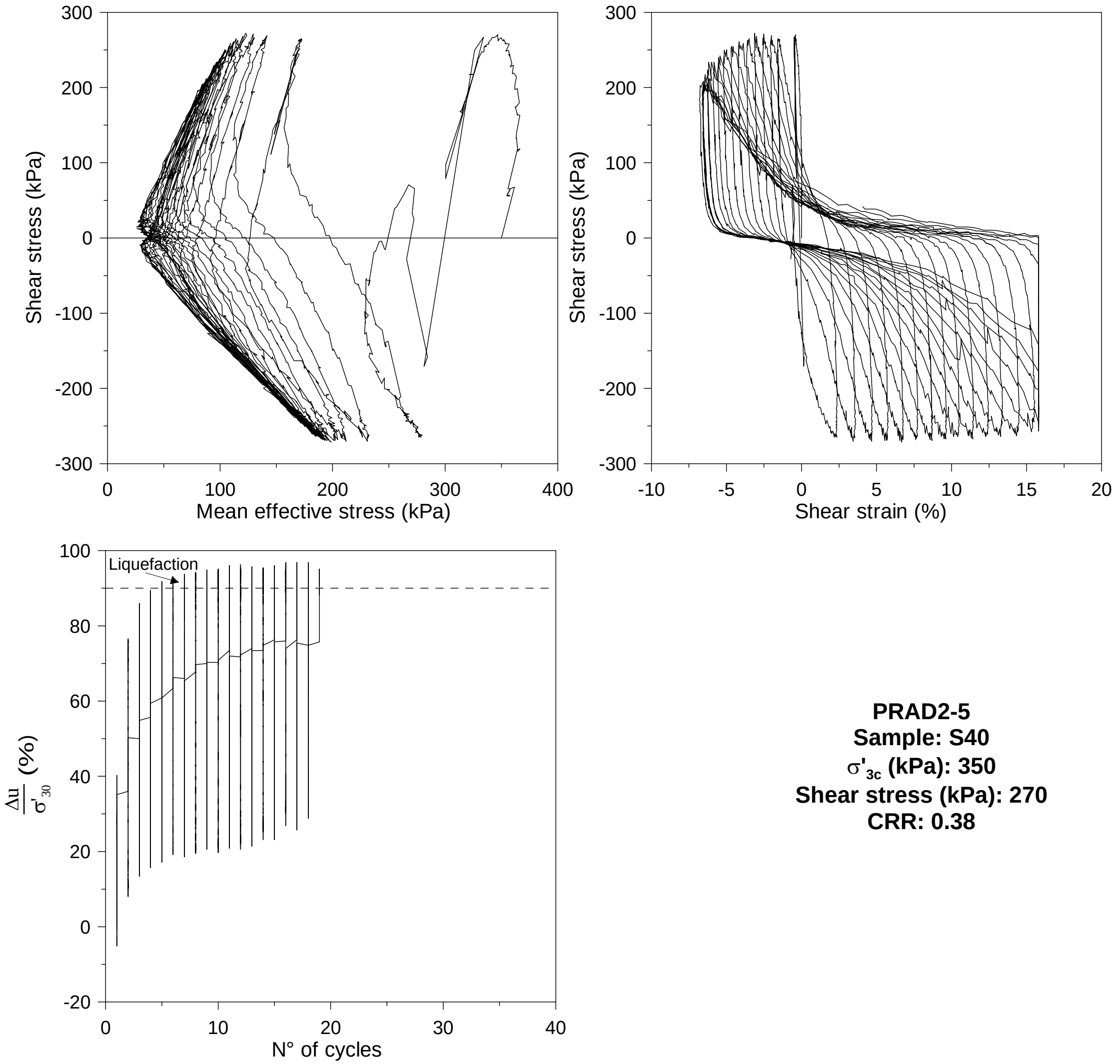

PRAD2-5
Sample: S40
σ'_{3c} (kPa): 350
Shear stress (kPa): 270
CRR: 0.38

Figure A5.